APPLICATIONS OF STRUCTURED LIGHT TO 3D SURFACE TOPOGRAPHY USING MOIRE PATTERN AND TO 3D IMAGING OF PHASE OBJECTS

Thesis

Submitted to

The School of Engineering of the

UNIVERSITY OF DAYTON

In Partial Fulfillment of the Requirements for

The Degree of

Master of Science in Electro-Optics

By

Haiyun Guo

UNIVERSITY OF DAYTON

Dayton, Ohio

August 2021

APPLICATIONS OF STRUCTURED LIGHT TO 3D SURFACE TOPOGRAPHY USING MOIRE PATTERN AND TO 3D IMAGING OF PHASE OBJECTS

Name: Guo, Haiyun

APPROVED BY:

Partha P. Banerjee
Advisory Committee Chair
Professor
Department of Electro-Optics and Photonics

Andrew Sarangan
Committee Member
Professor and Chair
Department of Electro-Optics and Photonics

Imad Agha
Committee Member
Associate Professor
Joint Physics and Electro-Optics Department

Cong Deng
Committee Member
Research Scientist
Department of Electro-Optics and Photonics

Robert J. Wilkens, Ph.D., P.E.
Associate Dean for Research and Innovation
Professor
School of Engineering

Eddy M. Rojas, Ph.D., M.A., P.E.
Dean, School of Engineering

ABSTRACT

APPLICATIONS OF STRUCTURED LIGHT TO 3D SURFACE TOPOGRAPHY USING MOIRE PATTERN AND TO 3D IMAGING OF PHASE OBJECTS

Name: Guo, Haiyun
University of Dayton

Advisor: Dr. Partha P. Banerjee

Three-dimensional (3D) reconstruction plays an important role in imaging research filed. Structured light technology has been widely used in 3D imaging, recognition and measurement, indicating great industrial and commercial value. In this thesis, a simple and robust technique of Moiré topography with single-image capture and incorporating digital filtering along with a four-step digitally implemented phase-shifting method is introduced for 3D surface mapping. Feature details in the order of tens to hundreds of microns can be achieved using interferometrically generated structured light to illuminate the object surface. The feasibility of this technique is verified experimentally, and applications to metallic surfaces are demonstrated. Next, a simple non-interferometric incoherent light propagation model is introduced to perform 3D profiling of transparent objects with typical thicknesses in the order of mm to cm by analyzing the distorted captured image behind the object. A two-dimensional (2D) cosine fringe is used as the incident reference image, whose periodicity is markedly altered by the shape of the object. By monitoring the local change in the period, the surface profile is simulated and optimized to achieve minimal error with experimental data to determine the final morphology. Besides, core principles of ghost imaging and optical scan holography are also discussed.

Dedicated to my parents

For their unconditional love all the time

ACKNOWLEDGMENTS

I would like to extend my deepest thanks to my advisor Prof. Partha Banerjee for his principal guidance and patient help for my study; warm concerns for my life; as well as careful instructions and significant support for my Ph.D. application. With his assistance, I not only completed my undergraduate and master's thesis, presented in OSA conference and published the journal, but also have improved my academic logical thinking, standard for experimental details and knowledge of the whole context of optical imaging. I would also like to thank our group members, Haowen Zhou and Dr. Mallik Hussain, for their fruitful discussions and important advice.

My sincere thanks to committee members, Prof. Andrew Sarangan, Prof. Imad Agha, and Dr. Cong Deng, for their professional academic guidance and constructive comments on this work, especially Dr. Agha for helping me with another research project. I want to thank my Huazhong University of Science and Technology (HUST) for my undergraduate education. Without the guidance of these excellent professors who taught me, I would not have found my motivation and ambition in the field of optoelectronics. I am grateful for the support of Department of Electro-Optics and Photonics, and School of Engineering at University of Dayton (UD), especially the HUST and UD 3+2 joint program.

Last but not least, I would like to express my special thanks to my parents for their financial support and unconditional love, as well as my boyfriend Bowen Cai for taking care of my life and emotions during the epidemic. In particular, I want to thank myself for my perseverance and efforts over the past two years, for the confidence that has kept me going during some tough times, and for the strong goals that have sustained me.

TABLE OF CONTENTS

LIST OF FIGURES

LIST OF TABLES

LIST OF ABBREVIATIONS

1D	One dimensional
2D	Two dimensional
3D	Three dimensional
AM	Additive manufacturing
BS	Beam splitter
CCD	Charged coupled device
FPP	Fringe projection profilometry
FT	Fourier Transform
HOPG	Highly oriented pyrolytic graphite
IFT	Inverse Fourier transform
LS	Laser sectioning
M	Mirror
MT	Moiré topography
OSH	Optical scanning holography
PSDH	Phase shifting digital holography

PUMA	Phase unwrapping max-flow algorithm
RMSE	Root mean square error
SNR	Signal-to-noise ratio
SP	Single-pixel
SPI	Single-pixel imaging
TIE	Transport of intensity equation
WYSIWYG	What you see is what you get

LIST OF NOTATIONS

$a_o(x,y)$	Background intensity of deformed pattern
$a_r(x,y)$	Background intensity of reference pattern
$b_o(x,y)$	Amplitude modulation distribution of deformed pattern
$b_r(x,y)$	Amplitude modulation distribution of reference pattern
$C_{1,1}, \dots, C_{M,N}$	Corresponding Fourier coefficients of $P_{1,1}, \dots, P_{M,N}$
d	Distance from camera to the beam splitter BS2
e	Ellipticity
f_0	Spatial frequency of the sinusoidal pattern
$f_X(x)$	Periodic extension of a function $f(x)$ with a period X
$f\#$	F-number
F_n	Fourier coefficients of $f_X(x)$
$FT\{\cdot\}$	Fourier transform
h	Depths/Heights
h_B	Distance from point B to the object's flat surface
$h_{obj}(x,y)$	Height of semi-circular cylinder

H	Distance from the flat surface to the imaging plane
k_{x0}	Spatial frequency of the reference cosine pattern along *x*-axis
k_{y0}	Spatial frequency of the reference cosine pattern along *y*-axis
L	Distance from the camera to the surface of the object
n_1	Refractive index of air
n_2	Refractive index of the transparent object
$N_{A/B}$	Normals passing through point A/B
$I_r(x,y)$	Reference structured light in Chapter II
$I_{ref}(x,y)$	Reference structured light in Chapter III
$M^{\pm}(x,y)$	Envelope (or beat or Moiré) pattern via addition/subtraction
$M_n^{+}(x,y)$	Moiré pattern with successive initial phase shifts $n\Delta\varphi$
$P_{1,1}, \ldots, P_{M,N}$	$M \times N$ 2D sinusoidal structured light patterns
α	Incident angle
β	Angle of refraction in the air
θ	Angle between the $\boldsymbol{K}$-vector of the fringes and the x-axis
θ_c	Critical angle
Λ	Actual period of the cosine fringe

$\varphi_o(x, y)$	Phase of the deformed pattern
$\varphi_r(x, y)$	Phase of reference pattern
$\Delta\varphi(x, y)$	Phase difference between deformed and reference images
$*$	Convolution operation

CHAPTER I

INTRODUCTION

1.1 Optical 3D Reconstruction

Three-dimensional (3D) objects make up this colorful real world. The accurate description and reconstruction of their morphology have always been one of the top research areas [1-10]. Starting from the 1850s to the present, the rapid development of various technologies has given rise to a wide variety of optical measurements to characterize various objects, ranging from phase objects, complex objects, objects with surface topgraphy, and 3D objects, and at different scales of dimensions. Along with their higher accuracy and faster speed, more and more advanced 3D measurement techniques have brought tremendous innovation and development to the manufacturing industry [2-4], culture and entertainment [6], precision instruments [7], aerospace [8], and other domains [9].

The 3D reconstruction system that combines optics, electronics, mechanical control, and computer data processing has gradually become the mainstream of industry, security and commerce, and will continue as their inevitable future trend [9,10]. Based on these kinds of systems, higher accuracy, faster speed, more extended detection range, and more measurement perspectives can be expected soon.

In the acknowledged traditional classification of 3D measurement, there are two broad categories: contact-type and non-contact-type. Although contact-type has good precision (in micron level), its cost and its limitation that it cannot be applied to soft objects are still significant issues. These issues can be avoided in non-contact-type measurements [1,11]. Moreover, with the wide application and rapid progress of optical and electronic components, non-contact technologies can improve resolution and working efficiency, and achieve a level of indeed high

precision. Consequently, most modern optical 3D measurements are non-contact and can be coherent or incoherent [12-18], which will be discussed later. Although much of the literature illustrates these two types with some typical specific methods respectively, there could be some which cannot be explicitly classified as above which have evolved with the development and integration of technologies.

In what follows, a few common non-contact 3D reconstruction technologies with their own advantages and limitations are introduced. Digital holography [19,20], computer vision [21-23], and structured light methods [24-26] have been studied extensively. These techniques have found applications in numerous fields, such as complex impeller and blade surface detection, human oral cavity and dental pattern measurement, plastic surgery effect evaluation [7], automobile detection, copying or profile modeling of various material objects, etc. Some innovative ideas, such as metalenses-based holography [27] and Surface plasmon resonance imaging [28], have also attracted researchers' attention in recent years for sub-wavelength imaging.

It is important to note that optical 3D reconstruction is different from machine vision, which focuses on mathematical models and algorithm optimization [22,23]. In contrast to machine vision, optical approaches rely on the optical theories of light ray/wave propagation and physical principles, such as refraction and reflection laws, Fresnel diffraction, transport of intensity (TIE) equation [29], polarization properties, etc. The integration of experimental systems and numerical calculations can bring more flexibility and make up for each other's shortcomings. Also, with the explosion in computing power, some processes involved in optical 3D reconstruction have changed from physical to digital, such as the transition from traditional holography to digital holography. Very recently, the introduction of neural networks and deep learning has led to further improvements in speed and accuracy [30,31]. To sum up, complementing digital techniques with physical experimentation and vice-versa is the path forward to achieve higher goals. Therefore, computational optical imaging has become a research hotspot in recent years.

1.2 Computational Optical Imaging and Structured Light Method

Computational imaging has dramatically changed the traditional "WYSIWYG (what you see is what you get)" imaging model [32-34]. Imaging has now changed from “point and shoot” to “shoot and point”. This needs special optical illumination or imaging systems, such as structured light illumination, aperture coding, optical transfer function modulation, controllable and removable detectors, etc. At this point, the captured image has already been modulated and often cannot be used directly, due to the additional optical coding introduced. But through a digital decoding process that goes with it, the ideal scene can be reconstructed.

Computational optical imaging gives traditional methods many revolutionary advantages that are difficult or even impossible to achieve on their own. For instance, computational techniques improve the quality of imaging (e.g. SNR, contrast and dynamic range) [34], simplifies the imaging system (e.g. no lens, smaller volume, lower cost), and breaks through the physical limitations of optical systems and image acquisition devices (e.g. resolution, field of view, imaging dimension) [33]. In general, it makes the imaging system significantly improved in terms of information acquisition ability, applied function, performance indexes, such as phase, coherence, 3D morphology, depth of field extension, blur restoration, refocus, and so on [32-34].

The structured light method, categorized as active triangulation, has grown rapidly and received wide acceptance among the existing methods for 3D visualization [24-26]. As a significant branch of computational optical imaging, it is an advanced technology that combines optical system with coding and image processing. The designed light points, strips or smooth surface structures [24,35,36], which are controllable, are projected to the object under interrogation. Depth information of the object is encoded into the deformed images recorded by optical imaging devices (such as a CCD camera). The captured images should be digitally processed to calculate the desired 3D data of the target, which is also known as decoding process.

The structured light method has the following merits:

(1) it is easy to implement;

(2) phase shifting, fringe density and direction change can be realized numerically without physical translations;

(3) it is fast, and enables a full-field inspection and measurement, and

(4) it can have high resolution and accuracy.

Because of these advantages, the structured light method has been commercialized in the coordinate measurement, gaming, and machine vision industries [24,25].

1.3 Ghost Imaging

Fringe projection profilometry (FPP) [37-40], a surface structured light technique, has been extensively investigated in connection to 3D topography from the reflected optical field. Moiré profilometry (also called Moiré topography) is an effective reconstruction approach in FPP [41,42]. A single-shot digital phase-shifting Moiré patterns method for 3D topography has been proposed and applied to mapping the surface topography of 3D metallic objects. This was part of my work during the HUST-EOP BS-MS program. Details are described in Chapter 2.

In this research, a lot of spectral analysis work has been done, which stimulated our interest in a comparatively new field named ghost imaging [43-46]. The process of illuminating an object with structured light, e.g., a periodic pattern which can be as simple as a sinusoidal variation, is similar to the concept of ghost imaging. While structured light with varying phase shifts can be used to scan the surface under investigation, the entire surface can also be alternatively interrogated using harmonics of the sinusoidal variations. If the light scattered from the surface illuminated by every element of a set of orthogonal waveforms is collected, the surface topography can be reconstructed by using this information and knowing the underlying “key” which is the set of orthogonal functions.

For simplicity, the one-dimensional (1D) case is taken as an example. Let $f_X(x)$ represent the periodic extension of a function $f(x)$ with a period X. Then the function can be represented by a series of orthogonal functions, such as a Fourier series in the form:

$$f_X(x) = \sum_n F_n \, exp(j2\pi nx/X), \tag{2-1}$$

where the Fourier coefficients F_n are given by

$$F_n = \frac{1}{X}\int_0^X dx \, f_X(x) exp - (j2\pi nx/X). \tag{2-2}$$

Using (2-1) and (2-2),

$$f(x) \sim f_X(x) = \sum_n \left(\frac{1}{X}\int_0^X dx' \, f_X(x') exp - (j2\pi nx'/X)\right) exp(j2\pi nx/X). \tag{2-3}$$

Equation (2-3) provides the recipe for reconstructing the "ghost" function $f(x)$ knowing the "Fourier" coefficients. One can look at the Fourier coefficients to be indicative of the integrated "energy" from the object $f_X(x)$ (detected by the "bucket" detector) multiplied (illuminated) by the set of functions ("known" patterns or keys) $exp - (j2\pi nx/X)$. The integrated energy can be collected by a lens with the detector at its back focal (or Fourier) plane.

The preliminary introduction above points out the core of ghost imaging. By an extension of this logic, Fourier series is not the only choice to recompose the function under test. Some "orthogonal" non-sinusoidal functions such as Bessel functions, Legendre functions, etc. can also be regarded as the bases. The essence of this "orthogonality" is spatial independence, which means that one function cannot be expressed in terms of other functions that have already acted as bases. Furthermore, any random masks which are orthogonal to each other as defined in a suitable function space can be used to illuminate the object, like binary random dots. [24] As long as the coefficient of each base to make up the target can be obtained; the superposition of each term should form the reconstruction.

Similarly, this concept can be extended to two-dimensions. In addition to 2D Fourier series, other 2D orthogonal functions such as functions with "angular momentum" of the form $\exp jn\theta$, Hadamard transforms, etc. can be applied [35,47,55]. It is worth noting that the number of these bases has to be large enough, otherwise the reconstructed "ghost" function would lose some information, resulting in large errors from the real answers.

Our idea happens to be similar to the Fourier single-pixel (SP) imaging technique [47]. For 2D image restoration, it has been proposed that the Fourier transform provides a perspective that an image consists of a weighted sum of harmonic 2D structured light patterns like cosine fringes with different frequencies. The illustration of this process is shown in Figure 1-1.

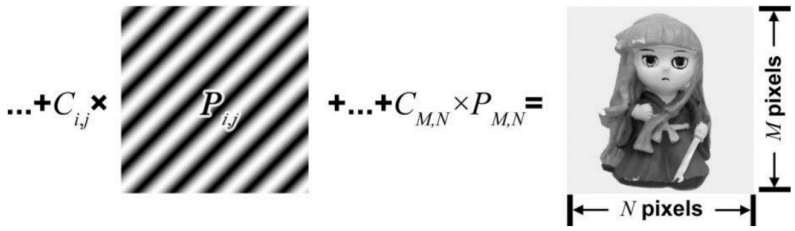

Figure 1-1: Illustration of 2-D Fourier transform [47]. A $M \times N$ digital image in the spatial domain can be expressed as a weighted sum of $M \times N$ 2D sinusoidal structured light patterns (i.e., $P_{1,1}, \dots, P_{M,N}$) by the corresponding Fourier coefficients, $C_{1,1}, \dots, C_{M,N}$.

Based on this principle, the typical image "cameraman" has been used to test the principle. The target image is originally $256\ pixels \times 256\ pixels$. After trying different numbers of 2D cosine images orthogonal to each other as bases, it has been found that $256 \times 256 = 65536$ references with varied periods are needed to obtain a clear reconstruction result as shown in Figure 1-2.

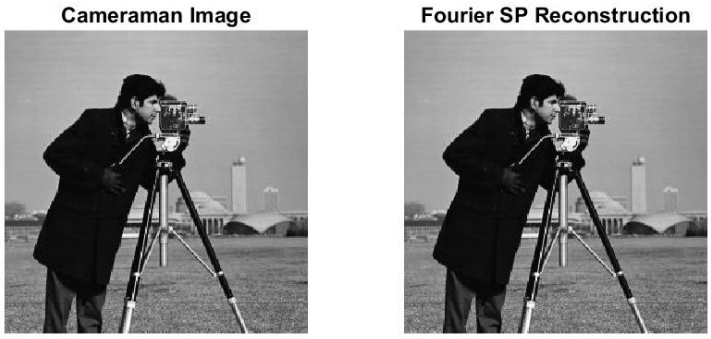

Figure 1-2: Illustration of "cameraman" image reconstruction by using Fourier based single-pixel (SP) imaging technique.

Each coefficient ($C_{M,N}$ in Figure 1-1) is derived by the sum of the product of each pixel of the corresponding base and the target. In optics, this "sum" could be achieved by a focusing lens and recorded by a bucket detector placed in its back focal plane [43]. Moreover, all detectors can only collect intensity information, that is $\left|C_{M,N}\right|^2$, so the coefficient calculation requires the square root of the detected data. After that, the reconstruction is digitally accomplished by multiplying each coefficient by its respective base and summing them up. Since the illumination is assumed as uniform here and the target is a transmissive image without any phase information, the operation of "square root" has little impact, and is only reflected in the contrast of the result. The general case of a complex $C_{M,N}$ is discussed further below.

Meanwhile, the same number of binary random dot images have also been applied as bases in the single-pixel imaging (SPI). The result, shown in Figure 1-3, is noticeably less sharp than in Figure 1-2. However, on the same computer, this simulation took only 171 seconds, compared to 1210 seconds for the case of the cosine fringe case, which is a difference by an order of magnitude.

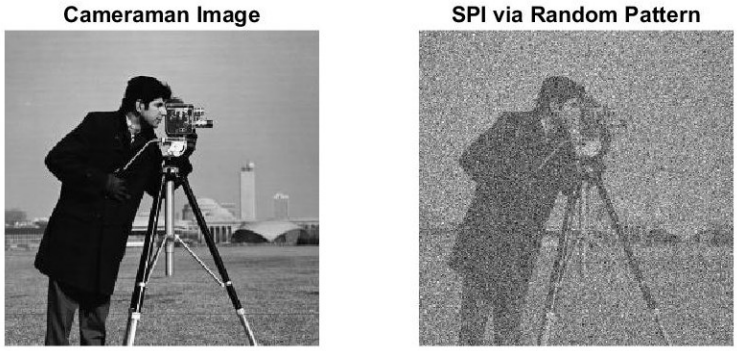

Figure 1-3: Illustration of "cameraman" image reconstruction by using single-pixel imaging (SPI) using binary random dot images.

After further investigation, we have found that ghost imaging technology can be greatly limited by the resolution and time-cost. When the amount of base images is not sufficient, the resulting quality clearly suffers. On the other hand, the number of bases for high-quality imaging is too large. Taking the above "cameraman" as an example, this $256\,pixels \times 256\,pixels$ reconstruction requires 65536 reference images. The recording time might last for tens of minutes or even hours in an actual experiment, and maintaining a stable low-noise environment is necessary but difficult during this period.

Another important thing to note is that ghost imaging technique may not work satisfactorily for transparent phase objects [48,49]. The bucket detector only records intensity information, which is the square of the absolute value of the light field. In other words, phase information is lost. For phase objects, it is more likely that the "Fourier" coefficients will be complex; thus, inability to collect phase information implies that the morphology of the 3D transparent phase object cannot be accurately computed using a simple bucket detector.

To collect phase information using a single pixel detector, as in the case of constructing a *complex* hologram, techniques used in optical scanning holography (OSH) has been examined [50-53]. OSH is a technique in which holographic information of a 3D object can be acquired by using a single 2D optical scan where scattered light from the object is detected by a photodetector.

However, such an optical scanning system cannot manipulate any phase information. Because holography requires the recording of the phase, one needs to find a way to preserve the phase information during photodetection in order to use optical scanning to record holographic information. The solution to this problem is optical scanning heterodyning. Here, the object is scanned by a time-dependent Fresnel zone plate, which is the superposition of a spherical wave and a plane wave of different temporal frequencies. The temporal frequency difference Ω between the two waves can be provided by using an acousto-optic modulator or an electro-optic modulator in the path of the plane wave. A lens is used as a light collector that collects all of the transmitted light to the photodetector. The complex information of the object is carried by the heterodyne frequency. To extract this information, one can electronically mix the heterodyne current with a sine and a cosine function at the heterodyne frequency to obtain the in-phase and the quadrature components of the current, respectively, and thereby compose the complex hologram.

An alternative to OSH to determine the complex "Fourier" coefficient can be to use a CCD array around the focal plane, and employ the principle of the TIE to determine the on-axis phase at the Fourier plane. This, however, needs a CCD instead of a single-pixel detector and translation around the focal plane. This will be investigated in the future.

1.4 Research Objectives and Organization of the Thesis

This thesis comprises a summary of work started during the undergraduate study at HUST involving the application of structured light method, which is a popular field in computational optical imaging as well as gaming. 3D reconstruction of both reflective and transparent objects will be demonstrated based on different techniques. First, a very straightforward and robust experimental set-up has been proposed to realize the reflective surface reconstruction. Based on this work, and inspired by simple principles of light bending when it travels through media of different refractive indices, a simple, convenient, fast and inexpensive system is designed to reconstruct transparent objects. Also, as outlined above, techniques such as ghost imaging,

Fourier SPI and OSH have been examined, and its connection with the structured light method has been investigated.

The thesis is divided into four Chapters. In Chapter I, the development background and market applications in optical 3D reconstruction and measurement have been introduced. The advantages and prospects of computational optical imaging have been outlined, and the concept of the structured light method has been explained. The principle of another technique named ghost imaging has been presented with selected simulations. Alternative methods such as OSH and TIE have been introduced.

Chapter II describes a single-shot digital phase-shifting Moiré pattern method for 3D topography and its application in surface reconstructions of two typical metallic objects. Moiré topography, a branch of FPP from the structured light method, has been specifically illustrated. The theoretical calculations, experiments, and analysis of simulation and experimental results, along with error calculations, have been presented in detail.

In Chapter III, the theoretical simulation and reconstructions of three transparent products with different morphologies have been demonstrated using structured light and a simple concept of light bending due to change of refractive index and curvature of the interface. Extensive error analysis has been performed to verify the correctness and accuracy of the technique. Moreover, the extension of this method to arbitrary phase objects has been explored for possible future work.

Chapter IV concludes the thesis with a summary of work performed and projections for future work.

1.5 Publications

Two conference presentations and one journal paper have resulted from this thesis work. These are listed below:

1. **H. Guo**, H. Zhou, and P. P. Banerjee, "Single-shot digital phase-shifting Moiré pattern for 3D metallic surface imaging," Digital Holography and Three-Dimensional Imaging Conf. HF3G-3 (2020).
2. **H. Guo**, H. Zhou, and P. P. Banerjee, "Single-shot digital phase-shifting Moiré patterns for 3D topography," Appl. Opt. **60**, A84-A92 (2021).
3. **H. Guo**, H. Zhou, and P. P. Banerjee, "Surface shape reconstruction of transparent objects using structured light," Digital Holography and Three-Dimensional Imaging Conf. (2021).

CHAPTER II

APPLICATION OF MOIRE PATTERNS TO 3D SURFACE TOPOGRAPHY

As discussed in Chapter I, the structured light method has been widely used in 3D object reconstruction due to its many advantages. In this Chapter, a simple and robust technique of Moiré topography with single image capture and incorporating digital filtering along with a four-step digitally implemented phase-shifting method is introduced for 3D surface mapping. Feature details in the order of tens to hundreds of microns can be achieved using interferometrically generated structured light to illuminate the object surface. Compared to the traditional optical phase-shifting method, a digital phase-shifting method based on Fourier processing is implemented with computer-generated sinusoidal patterns derived from the recorded deformed fringes. This enables a single capture of the image which can be used to reconstruct the 3D topography of the surface. Single shot imaging is simple to implement experimentally and avoids errors in introducing the correct phase shifts. The feasibility of this technique is verified experimentally, and application to metallic surfaces are demonstrated.

2.1 Introduction

Optical 3D imaging techniques have been extensively implemented in industrial inspection [2], quality monitoring [3,4], biomedicine [5], television entertainment [6], and many other fields during the past thirty years [7-10]. 3D imaging can be achieved using one-dimensional spatial scanning [12-14], 2D recording to reconstruct the 3D information of the target object [15,16], range gating and time of flight measurements as in LiDAR [17], etc.; a review of various methods can be found in Chen *et al.* [18]. After a comprehensive analysis of their characteristics, combined with the features of the objects in our work, such as the reflectivity of metallic surfaces, small feature

sizes (in the order of tens to hundreds of microns), ease of implementation, etc., the structured light method has been chosen.

The structured light method has grown rapidly and received wide acceptance among the existing methods for 3D visualization, since it is fast, easy to implement, with a large field of view, high resolution and accuracy [24-26]. Different forms of the light sources and patterns have been used for structured light, viz., laser sectioning (LS) [14,54], FPP [37-40], and other coded forms of plane structured light projection [35,55]. Due to limitations of LS based on the reflectivity of the surface material, and because of the simplicity of fringes in various encoding forms and measurement efficiency, FPP is regarded as a more common image processing algorithm, with Moiré topography (MT) as a representative approach [41,42].

A Moiré pattern is a beat pattern produced by the superposition of two almost identical or similar periodic patterns. MT is based on the generation and processing of Moiré patterns. Incoherent white light is usually used as the light source to project the fringe-like pattern onto the object surface. The phases of the pattern are modulated by the height profile of the object to yield deformed fringes. The height information can be extracted by analyzing the Moiré pattern formed between the illuminating and the reflected fringes. The resolution depends greatly on the number of fringes [56].

MT has undergone many technical developments. Depending on the system structure, MT can be broadly categorized as shadow Moiré method or projection Moiré method [57,58]. However, both methods place the actual gratings in the optical path for the direct physical overlap. The optical superposition results in low contrast of Moiré patterns and unsatisfactory filtering effect; thus, a digital Moiré pattern method has been proposed [59,60]. The digital Moiré pattern is achieved by digital projection of two fringes and reconstructing the phase information from captured images numerically. This improvement, inspired by optoelectronic imaging (viz., CCD arrays) and digital processing techniques, results in the advantages of a simplified system, strong

anti-interference and flexibility in adjusting fringe structures. Furthermore, the ability to generate finer and lower noise fringes provides higher sensitivity and spatial resolution that can be demonstrated by its capability of deformation measurement in tiny zones. Hence for objects with feature sizes in the scale of tens to hundreds of microns, the use of digital Moiré pattern method is of advantage.

FPP can extract the phase/height information by computing the intensity image of Moiré patterns via two mainstream algorithms: the phase-shifting method and the Fourier transform method [61]. With multiple captures of images, the phase-shifting technique is insensitive to changes in surface reflectivity and ambient light, which brings great convenience in reconstructing complex surface shapes, and a pixel-level accuracy by point-to-point measurement [62-65]. The Moiré pattern technique, combined with the phase-shifting method, has found applications in lattice structure analysis, and strain field measurement of various materials such as heterostructure interfaces [66], MEMS deformation behavior [67], and residual deformation of highly oriented pyrolytic graphite (HOPG) [68] because of the magnifying effect on small differences in the structure under investigation. This method approximates the intensity distribution of the Moiré fringes as a trigonometric function which includes the unknown object phase in its argument, which is then calculated using the phase shifting technique. The Fourier transform method [61] is fast and relies on multiplying the Moiré fringes by the complex conjugate of the carrier to derive the phase. In our work, a hybrid technique based on Fourier processing is employed to find the Moiré pattern and subsequent phase shifting to determine the phase map, and hence, the topography of the surface.

Specifically, in this work, a simple and robust single-shot digital phase-shifting Moiré technique is introduced. To provide adequate resolution, the period of the laser interference fringes can be readily changed by adjusting the angle between the interfering beams. These fringes, acting as the reference light source, are projected to the surface being interrogated and the

reflected light pattern is recorded by a commercial camera. Note that this is still a non-interferometric measurement technique, since the interference fringes are only used as a programmable illuminating structured light source. Thus, it is similar to using a projector to produce a designed sinusoidal pattern; however, the use of interference patterns can generate denser and more adjustable fringes. Now, multiple shots in the usual phase-shifting technique have a major issue in introducing exact optical path differences or phase shifts. A digital phase-shifting method is therefore utilized in our technique to avoid introducing phase shifts optically. Reference images with different shifts can be generated by finding the spatial frequency of the (near) sinusoidal pattern in Fourier domain from the reflected light off the surface under interrogation and phase shifts can be digitally incorporated in the spatial domain. By combining interferometric MT and precise digital phase-shifting, which efficiently generates references via simple spectral analysis, our single-shot technique provides a novel approach to 3D topography of metallic objects of micron feature sizes.

In this Chapter, Section 2.2 introduces the theory of our method. Experiments for a metallic surface such as a Newport logo on a screw head and 3D additive manufacturing (AM) product is been presented in Section 2.3, along with a detailed error analysis. In Section 2.4, remarks of this work are concluded, and future works are discussed.

2.2 Methodology

2.2.1 Generation of Moiré pattern

As a simple demonstration of the principle, a sinusoidal intensity pattern of light is used, which is conveniently generated from the interference of collimated beams, considered to be plane waves for simplicity. This allows for the fringe period to be readily changed by changing the angle between the interfering beams. In reality, more complicated (periodic) patterns can be generated using specialized gratings. Theoretically, periodic fringes of any shape can be decomposed into

the superposition of sine and cosine fringes with varying spatial frequencies and their harmonics by using Fourier series. To give a straightforward interpretation, a simple case of a one-dimensional sinusoidal intensity fringe pattern is used in the following theoretical analysis. Thus, the reference structured light can be expressed as:

$$I_r(x,y) = a_r(x,y) + b_r(x,y)\,cos[2\pi f_0 x + \varphi_r(x,y)], \tag{2-1a}$$

and the light from the object with deformed fringes can be presented as

$$I_o(x,y) = a_o(x,y) + b_o(x,y)cos\,[2\pi f_0\, x + \varphi_o(x,y)], \tag{2-1b}$$

where f_0 is the spatial frequency of the sinusoidal pattern; $a_{r,o}(x,y)$ and $b_{r,o}(x,y)$ represent the background intensity and amplitude modulation distribution of the fringes, respectively. $\varphi_r(x,y)$ denotes the phase of reference pattern; $\varphi_o(x,y)$ is the phase of the deformed pattern which contains the surface shape information of the object. According to Euler's formula, Eqs. (1a) and (1b) can be rewritten as:

$$I_r(x,y) = a_r(x,y) + \frac{1}{2} b_r(x,y)\,exp[i(\varphi_r(x,y) + 2\pi f_0 x)]$$

$$+\tfrac{1}{2} b_r(x,y) exp[i(-\varphi_r(x,y) - 2\pi f_0 x)], \tag{2-2a}$$

and

$$I_o(x,y) = a_o(x,y) + \frac{1}{2} b_o(x,y)\,exp[i(\varphi_o(x,y) + 2\pi f_0 x)]$$

$$+\tfrac{1}{2} b_o(x,y) exp[i(-\varphi_o(x,y) - 2\pi f_0 x)]. \tag{2-2b}$$

The phase difference $\varphi_o(x,y) - \varphi_r(x,y)$ is directly related to the height/depth information. The relation can be approximated by a linear transform [69]. The addition of two intensity images is to generate a Moiré pattern. The desired signal is obtained after band-pass filtering in the spatial frequency domain. To see this, note that the spectrum of the addition/subtraction of the two

intensities in Eqs. (2-2a) and (2-2b), leaving out the explicit dependence on (x, y) for brevity, can be expressed as:

$$FT\{I_r \pm I_o\} = FT\{a_r \pm a_o\} + FT\left\{\frac{1}{2}\left(b_r e^{i\varphi_r} \pm b_o e^{i\varphi_o}\right)\right\} * \delta(f_x - f_0)$$

$$+FT\left\{\frac{1}{2}\left(b_r e^{-i\varphi_r} \pm b_o e^{-i\varphi_o}\right)\right\} * \delta(f_x + f_0), \quad (2\text{-}3)$$

where $FT\{\cdot\}$ represents the Fourier transform and $*$ denotes convolution operation, and where the $\pm$ signs refer to addition and subtraction, respectively. By using an appropriate band-pass digital filter, the f_0 (or $-f_0$) component can be selected in the spatial frequency domain. Following an inverse Fourier transform (IFT), the result is multiplied with its complex conjugate. For example, if the spectrum centered around f_0 is acquired, the distribution in the spatial domain of the envelope (or beat or Moiré) pattern which contains the object phase $\varphi_o(x, y)$ can be expressed as:

$$M^{\pm}(x, y) = \frac{1}{4}\left({b_r}^2 + {b_o}^2\right) \pm \frac{1}{2} b_r b_o \cos(\varphi_o(x, y) - \varphi_r(x, y)). \quad (2\text{-}4)$$

Other arithmetical operations such as multiplication can also be applied to the reference and deformed fringes to form the Moiré pattern. Subtraction is almost identical to the above process, while the multiplication method is more involved:

$$FT\{I_r \times I_o\} = FT\left\{a_r a_o + \frac{1}{4} b_r b_o\left(e^{i(\varphi_o - \varphi_r)} + e^{-i(\varphi_o - \varphi_r)}\right)\right\}$$

$$+FT\left\{\frac{1}{2}\left(a_r b_o e^{i\varphi_o} + a_o b_r e^{i\varphi_r}\right)\right\} * \delta(f_x - f_0)$$

$$+FT\left\{\frac{1}{2}\left(a_r b_o e^{-i\varphi_o} + a_o b_r e^{-i\varphi_r}\right)\right\} * \delta(f_x + f_0)$$

$$+FT\left\{\frac{1}{4} b_r b_o e^{i(\varphi_o + \varphi_r)}\right\} * \delta(f_x - 2f_0) + FT\left\{\frac{1}{4} b_r b_o e^{-i(\varphi_o + \varphi_r)}\right\} * \delta(f_x + 2f_0), \quad (2\text{-}5)$$

and has the added complication of two additional components around the spatial second harmonic, viz., $\pm 2f_0$. Due to the difficulty in extracting the modulation around a certain spatial frequency due to possible overlapping of sidebands, addition serves as a better approach than multiplication. In our work, addition is used instead of subtraction or multiplication.

2.2.2 Digital phase shifting

A four-step phase-shifting method is used to extract the desired $\varphi_o(x,y) - \varphi_r(x,y)$ from Eq. (2-4), as in phase shifting digital holography (PSDH) [70]. Since the reference pattern is computer-generated in our method, $\varphi_r(x,y)$ can be set to a constant φ_r in subsequent calculations. The reference pattern can be produced by taking the Fourier transform of Eq. (2-2b), and determining the location of the first-order peaks in the spectral domain to find f_0. Further details on how the reference fringes are numerically generated in our experiment is described in Section 2.3.2. Successive initial phase shifts $n\Delta\varphi$ can now be digitally added to the cosine reference beam in Eq. (2-1). Thus, the distributions according to Eq. (2-4) can be re-expressed as

$$M_n^+(x,y) = \frac{1}{4}\left({b_r}^2 + {b_o}^2\right) + \frac{1}{2} b_r b_o \cos(\varphi_o(x,y) - \varphi_r - n\Delta\varphi). \tag{2-6}$$

With different values of n, viz., $n = 0,1,2,3$, and $\Delta\varphi = \frac{\pi}{2}$, the distributions M_0, M_1, M_2, M_3 can be obtained from Eq. (2-6) respectively (the superscripts + are omitted for simplicity). Then, the wrapped phase can be calculated by:

$$\Delta\varphi(x,y) = \varphi_o(x,y) - \varphi_r = arctan\left(\frac{M_3 - M_1}{M_2 - M_0}\right), \tag{2-7}$$

which is similar to PSDH [63]. On account of the arctangent function, the computed results of the phase for every pixel are restricted to $[-\pi, \pi]$. The true phase values, however, are normally beyond this range: a 2π jump may happen when the computed (or wrapped) phases come close to

$-\pi$ or π. Then, phase unwrapping max-flow algorithm (PUMA) is implemented to unwrap the phase [71]. Limitations of PUMA are mentioned in Zhou *et al*. [72].

2.2.3 System calibration

System calibration can be divided into two parts: horizontal calibration, which converts pixel coordinates to transverse length coordinates, and vertical calibration, also known as phase-to-height conversion. Horizontal calibration can be readily achieved by noting the actual dimensions of a part of the object and the number of pixels it occupies on the camera. The ratio between these two data is then used to calculate the true physical length represented by each pixel. Vertical calibration, however, is more complex, because different setups require different mathematical models [73-77]. As discussed below, under suitable approximations, it can be shown that the phase difference $\Delta\varphi(x,y) = \varphi_o(x,y) - \varphi_r$ is linearly proportional to the depth/height as briefly mentioned in Section 2.2.1, so that the unwrapped phase map obtained can be converted into a real 3D reconstruction of the topography of the object. In this work, a basic traditional triangulation system is applied [78], and the exact relation is given in Section 2.3.1 in accordance with the experimental setup.

2.3 Experiments and Results

2.3.1 Experimental setup

The experiment is set up on an optical table to minimize vibrations, and a dark environment is maintained to avoid stray light. Although structured light can be generated in many different ways [14,35,37-40,54,55], a Mach-Zehnder interferometer consisting of two mirrors (M1,2) and two beam splitters (BS1,2) is used to generate the sinusoidal fringes, as shown in Figure 2-1. Light from an Ar-ion laser with a wavelength $514.5\,\mathrm{nm}$ is collimated by the spatial filter and a collimation lens, then split into two parts by BS1. Reflection of the collimated laser beam from mirrors M1,2 recombines at BS2. The spatial frequency of the interference fringes can be changed

by slightly varying the angle of M1. Through measurement of the fringe density in our experiment, the angle between the two beams exiting BS2 is 0.92° (approximately 1 degree); however, the principle of using interference to generate the sinusoidal pattern enables the flexibility to change the fringe density as required depending on the desired resolution [79].

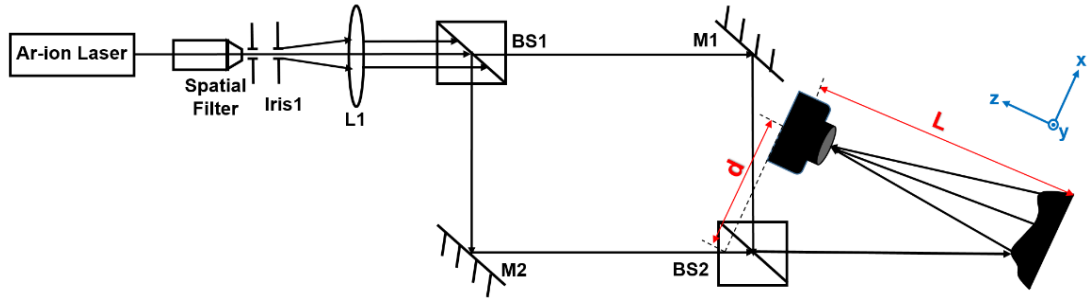

Figure 2-1: Schematic diagram of the optical system for single shot digital phase-shifting Moiré pattern technique. An Ar-ion laser with a wavelength of $514.5\ \text{nm}$ is expanded and collimated by a spatial filter assembly, including a $10\times$ microscope objective and 25-μm pinhole, and a collimation lens with a focal length of $250\ \text{mm}$. A Mach-Zehnder interferometer is used to generate the (co)sinusoidal pattern, which is projected onto the surface of the object. The distance from the camera to the surface of the object is L and the distance from camera to the beam splitter BS2 is d. L1: Lens; BS1,2: Beam splitters; M: Mirror. Inset: snapshot of illuminating fringe pattern. θ: Angle between the $\boldsymbol{K}$-vector of the fringes and the x-axis.

The interference fringes, with a spatial period in the order of a few hundred microns, illuminate the object surface at oblique incidence, as shown in Figure 2-1. Light scattered from the surface is imaged by a camera (Canon EOS 800D, 6000×4000 pixels, EFS $18-55\ \text{mm}$ lens) with optical axis normal to the object surface. The distance along the normal between the object and the camera is $L=250\ \text{mm}$, and the distance from the camera to the beam splitter (BS2) is $d=165\ \text{mm}$. It is ensured that the camera does not block the fringe pattern projected to the object surface; furthermore, its exact location is determined by its resolving power. After several trials, the optimum camera F-number is set to 6.3 and the optimum exposure time is chosen as $0.3\ \text{s}$ for best image quality.

Based on the coordinates in Figure 2-1, the object is placed in the x-y plane, and z-axis is perpendicular to the object and points to the camera. Considering the geometric construction

shown in Figure 2-1, the depths/heights derived from optical path analysis are computed via the vertical calibration equation [78]:

$$h = \frac{L\Delta\varphi}{2\pi[cos(\theta)]d/\Lambda+\Delta\varphi}, \tag{2-8}$$

where Λ represents the actual period of the cosine fringe and θ denotes the angle between the $\boldsymbol{K}$-vector of the fringes and the x-axis. The $cos\,(\theta)$ term has been added to the denominator to take into account the inclination of the fringes. Since L and d can be measured, h can be obtained from Eq. (2-8) using the value for $\Delta\varphi$ derived from Eq. (2-7). For $\Delta\varphi \ll 2\pi[cos(\theta)]d/\Lambda$ (which is true for our case), an approximately linear relationship results:

$$h = \frac{L\Lambda}{2\pi d[cos(\theta)]}\Delta\varphi. \tag{2-9}$$

2.3.2 Phase retrieval and topography of a metallic object

The object under interrogation is the surface of a metallic screwhead bearing the Newport® logo. According to the setup described above, the deformed pattern is recorded by the camera, only part of whose area is occupied by the target object, shown in the 1024×1024 pixels cropped image as Figure 2-2(a). The value of Λ in this experiment is 421.7 microns (corresponding to an angle of 0.92 degrees between the two beams in the Mach-Zehnder interferometer). The spectrum of an ideal cosine function with a DC bias consists of three delta (δ) functions separated in spatial frequency domain as the zeroth order, the positive and negative first-order components. Therefore, the reference fringe illuminating the object, which is regarded as an ideal cosine fringe, can be derived from knowledge of the location of the three impulses in the Fourier domain of the deformed fringe pattern. In Figure 2-2(b), the maximum peak is properly located at the center $(0,0)\ \mathrm{m}^{-1}$ with the value of 2.13×10^5, and the positions of two secondary peaks are $(-1.451 \times 10^4, 3056)\ \mathrm{m}^{-1}$ and $(1.451 \times 10^4, -3056)\ \mathrm{m}^{-1}$, with magnitudes of 2.24×10^4 for both peaks. From the location of the peak of the first-order spatial

frequency component, the spatial frequency of the reference cosine pattern along x- and y-axis, (k_{x0}, k_{y0}), can be determined. The cosine function can be expressed as $\cos(k_{x0}x + k_{y0}y)$. Figure 2-2(c) is the cosine pattern obtained. The angle θ in Eqs. (2-8,2-9) is 12.5° from our calculations.

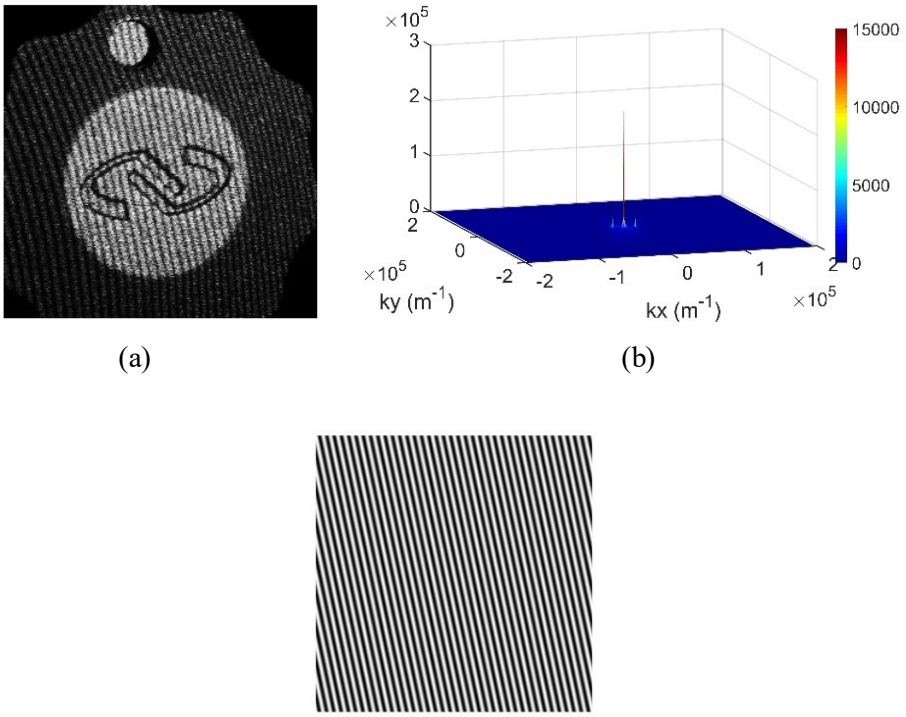

(a) (b)

(c)

Figure 2-2: (a) The cropped image from the image taken by the camera showing the region of interest; (b) the spectrum of (a); (c) the reference image without any phase shifts.

Using the information in Figure 2-2(c), cosine fringes with different initial phases $0, \frac{\pi}{2}, \pi, \frac{3\pi}{2}$ can be generated numerically to get the four reference patterns. The four Moiré pattern images referred to as $M_n^+(x, y)$ in Eq. (2-6) can be obtained from the superposition between the deformed fringe pattern and the four references, as shown in Figs. 2-3(a-d). In order to avoid spectral aliasing, the image is zero padded to a size of 2048×2048 pixels, which is twice as large as the

cropped image. As shown in Figure 2-3(e), a typical spectrum with three modulated components is presented.

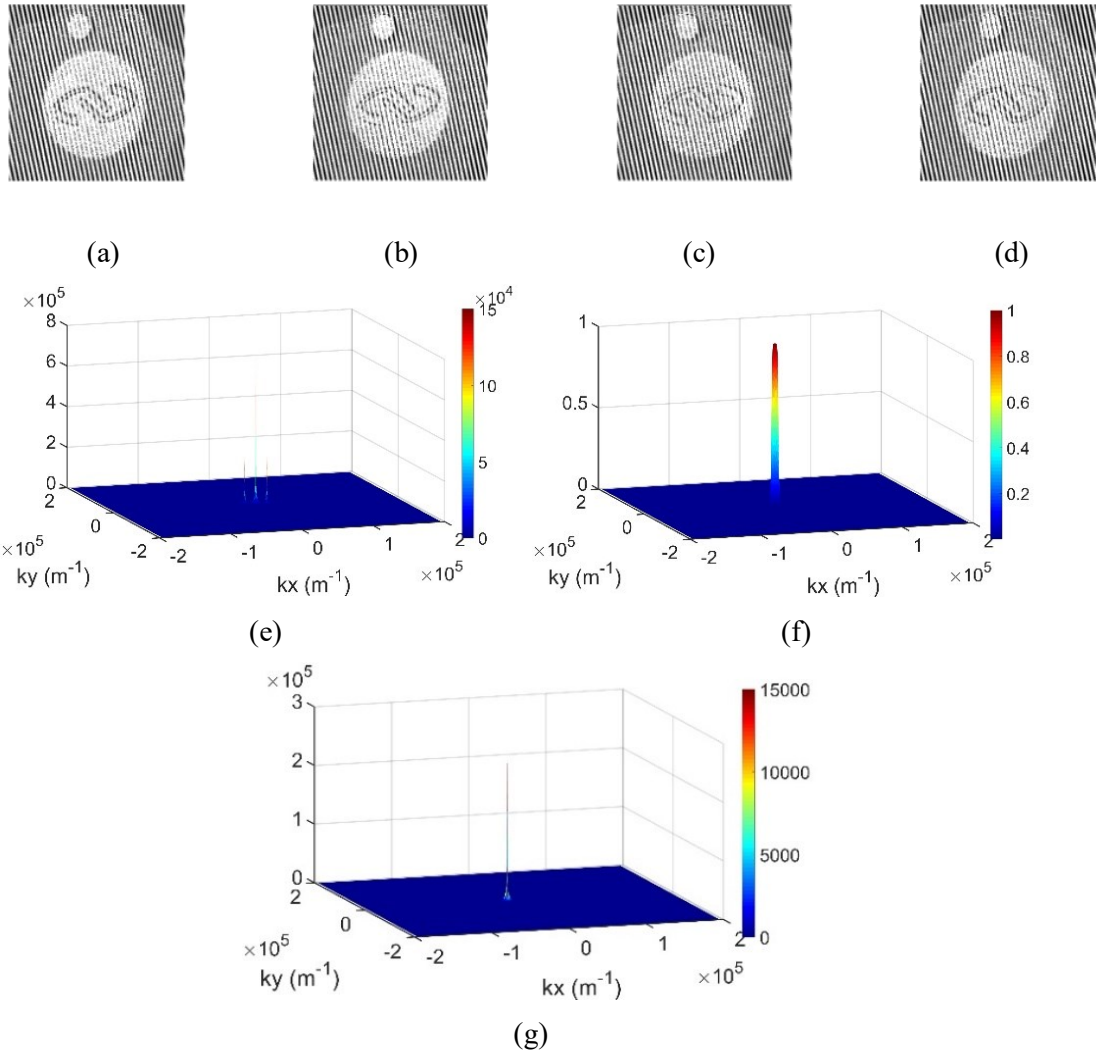

Figure 2-3: Superposed images containing Moiré patterns with digitally generated initial phase shifts (a) 0; (b) $\frac{\pi}{2}$; (c) π; (d) $\frac{3\pi}{2}$; (e) the spectrum of (a); (f) the designed band-pass Butterworth digital filter centered at one first-order spectrum; (g) the filtered component from (e) using the band-pass filter in (f).

After trying with different orders of Butterworth filters, it is found that the fourth-order performs the best in this case. The choice of fourth-order filter is based on the spectrum of the object surface. Accordingly, a fourth-order Butterworth digital filter with pass band centered at $(k_x, k_y) = (-1.451 \times 10^4, 3056)\ \text{rad} - \text{m}^{-1}$, as shown in Figure 2-3(f), is applied to the one of

the first-order components. The half-bandwidth is selected to be $4583.5\,\mathrm{rad-m^{-1}}$. The spectrum after filtering is shown in Figure 2-3(g). Then, IFT is performed to the filtered spectrum and its result is multiplied with its complex conjugate to get $cos(\varphi_o(x,y)-\varphi_r)$ in Eq. (2-4). A similar process can also be done for the Moiré patterns with different phase shifts to finally find M_0, M_1, M_2, M_3, respectively. Compared to a rectangular filter, Butterworth filter has a significant advantage in a nearly flat frequency response in the passband with smooth decay, and there is minimal ringing effect in the inverse domain.

The information of the object is derived from the phase of the Moiré pattern. By putting M_0, M_1, M_2, M_3 into Eq. (2-7), the wrapped phase is obtained, as shown in Figure 2-4(a). Note that outside the Newport logo, reconstruction is also obtained, namely a parabolic surface (see Figure 2-4(b)), as indicated by the outside fringes in Figure 2-4(a). The region that was previously air yields speckle or noise (see Figure 2-2(a)) and correspondingly Figure 2-4(a). Figure 2-4(b) demonstrates the unwrapped phase value of each pixel. The reconstruction area is adjusted to 800×800 pixels (from 100-900 pixels in both transverse dimensions) for a better view of the screwhead. The PUMA algorithm has been used for phase unwrapping. The length of the longer side of the logo on the surface is measured as $8\,\mathrm{mm}$ corresponding to 498 pixels, thus the pixel pitch based on the measurement is $16.06426\,\mu\mathrm{m/\,pixel}$. Equation (2-9) is then used to convert the phase to height, yielding the 3D reconstruction result shown in Figure 2-4(c). It is checked that the condition $\Delta\varphi \ll 2\pi[cos(\theta)]d/\Lambda$ is satisfied to ensure the validity of Eq. (2-9).

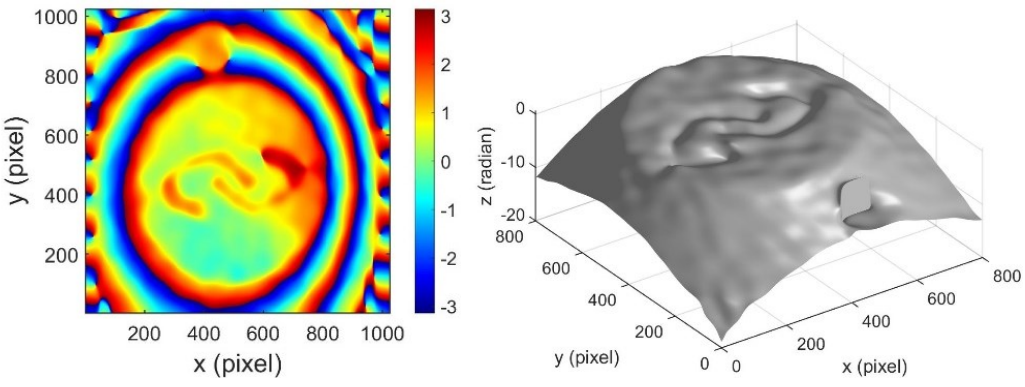

(a) (b)

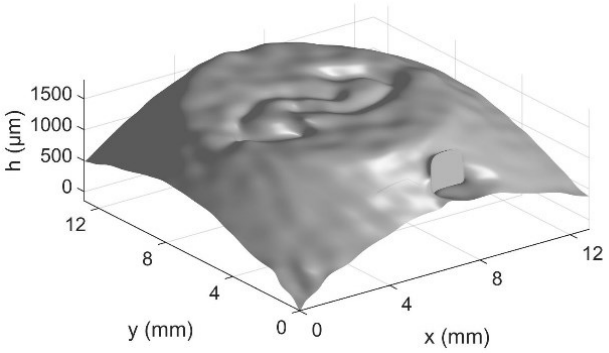

(c)

Figure 2-4: (a) The wrapped phase in $[-\pi, \pi]$ of the Newport logo; (b) the phase unwrapped by PUMA algorithm and displayed between 100-900 pixels in (a) in each dimension. For convenience, the axes have been marked from 0-800 pixels; (c) the 3D reconstruction of the Newport logo after system calibration.

2.3.3 Analysis of results

From preliminary visual observation, the profile and features of the logo in Figure 2-4(c), are qualitatively similar to the ground truth. In order to check the accuracy of the derived results, the surface is also analyzed using an advanced high precision optical microscope (Keyence VR5000) to obtain precise data through a line scan. From our experimental results, the recovered depth information one vertical line shown in Figure 2-5(a) is extracted as an example and plotted in Figure 2-5(b), while the line-scan of the same location via the microscope is shown in Figure 2-5(c).

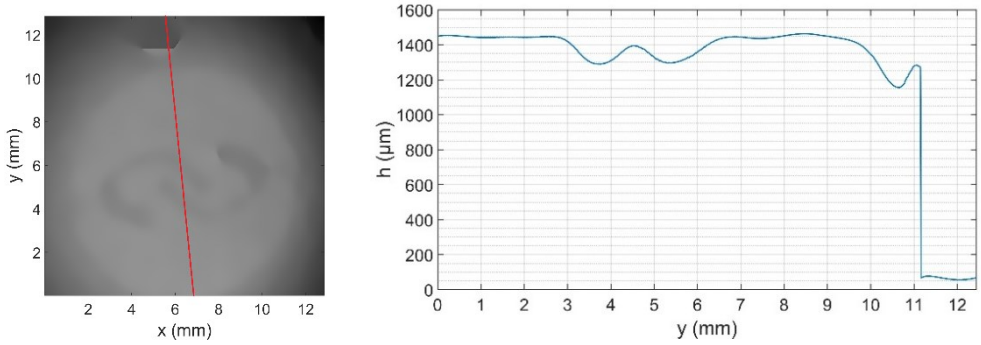

(a) (b)

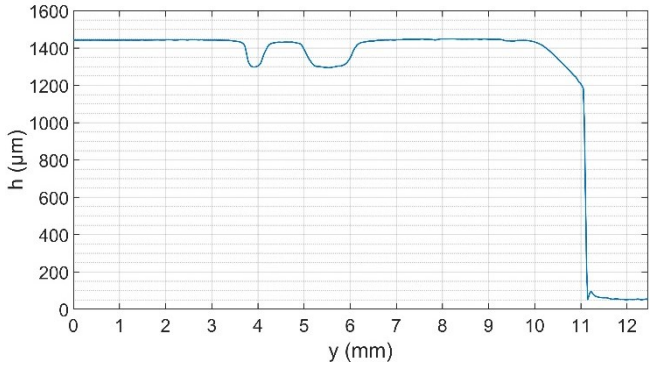

(c)

Figure 2-5: The verification of the accuracy of 3D topography using structured light: (a) the position of a line on the Newport logo used for comparison; (b) the depth profile along the line in (a), plotted as a function of y, obtained from retrieved phase and height using structured light; (c) precise data along the same line measured by optical microscope, also plotted as a function of y.

Typical depths of these two engravings of Newport logo in Figure 2-5(c) are both approximately 148 microns, which is in good agreement with our experimental results of around 154 and 149 microns, respectively, along y-axis. The average slopes, which are an artifact, are numerically eliminated, as shown in Figs. 2-5(b) and 2-5(c). The error of Keyence VR5000 is usually about $\pm 5\mu m$, provided by the datasheet. From our experiment, topographic profiles at a resolution of tens to hundreds of microns can be easily achieved. The topographic variations monitored using structured light are of the same order as those from the optical microscope, and with the added advantage of one-shot registration across a 2D surface without the need for scanning.

The spectral distribution is directly related to the fringe density. In this experiment, the distribution is still not separated enough in the Fourier domain and the first-order spectrum broadening is large, thus, some edge information in the first order may be overlapped with other spectral components (viz., around the 0^{th} order). Additionally, the engravings are very steep, therefore, the spatial frequency of theses information is very high, meaning that its spectral distribution is far away from the center of the first-order spectrum. However, the radius of the digital filter should not be too large, otherwise the noise as well as overlap from the zeroth order

will seriously affect the reconstruction quality. Therefore, the loss of the sharpness is an inevitable problem.

A discussion on the effect of noise is now in order. After a careful analysis of Figure 2-2(b), the noise level is calculated about 30 dB or more below the (sideband) signal level. In addition, contribution from vibrational noise is minimal in our experimental setup environment. In the experiment, the surrounding environment is completely dark, the instability of the operating platform is extremely little, and only one-shot measurement reduces the introduction of a lot of noise. More detailed analysis of the effects of different kinds and sources of noise will be pursued in the future.

2.3.4 Application to metallic additive manufacturing products

As a second illustration of the applicability (and limitations) of our technique, the structured light generated through interference is applied to reconstruct the topography of a small rectangular box constructed using laser AM. The object is smaller in size than the screwhead and a rougher surface finish. Using the same setup as described in Figure 2-1, the new values of L and d are $26\ \text{cm}$ and $16.5\ \text{cm}$, respectively, and the cropped image of target object is only 400×400 pixels. A similar process is implemented to reconstruct the surface topography of the AM object. The period of the cosine fringe illuminating the object (see Figure 2-6(a)) is $317.92\ \mu\text{m}$, as compared to 421.7 microns used for the screwhead with the Newport® logo. During processing of the spectrum, a sixth-order Butterworth digital filter with a half-bandwidth of $3055.7\ \text{m}^{-1}$ is designed for this case. Based on the revised experimental setup, the pixel pitch for horizontal calibration based on the measurement is $19.87\ \mu\text{m/ pixel}$.

The reason for a higher order filter choice for the AM case is that the speckle noise (scattering effect) from the AM sample is much more severe than screwhead case, thus, there is more undesired

spectral components over the entire spectrum. In order to minimize this, the filter design should have a sharper cutoff, as in higher order Butterworth filters.

As is clear from the 3D reconstruction of the surface topography shown in Figure 2-6(b), the general surface roughness is clearly visible; however, some of the detailed 3D profile information is lost, due to the rather large period of the illuminating fringe pattern compared to the scale of the surface roughness. As discussed earlier, resolution can be enhanced by increasing the fringe density, and is part of ongoing work. Once the optimum fringe density for a certain application is realized, this technique can provide an inexpensive and reliable way to perform 3D mapping of AM manufactured surfaces; however, even at its present status, the scale of the roughness can be readily monitored. For instance, from Figure 2-6(c), the standard deviation can be computed as approximately $80\ \mu m$, which is our estimate of the roughness of the finished AM surface.

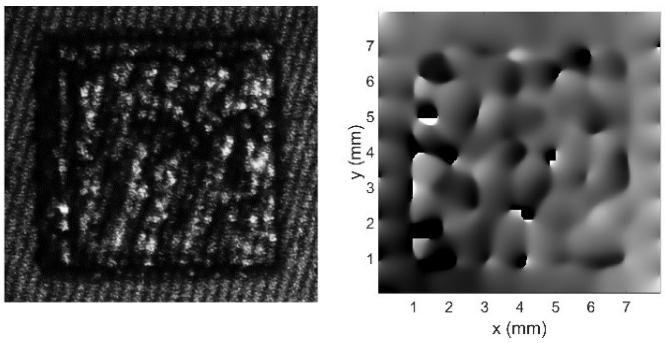

(a) (b)

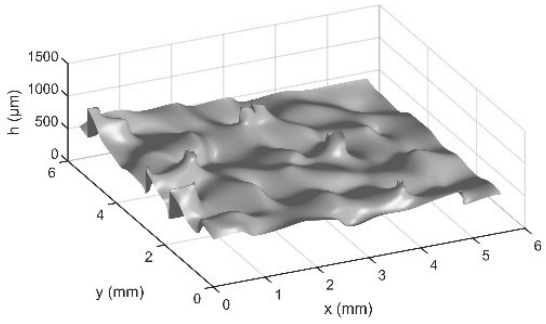

(c)

Figure 2-6: (a) Recorded image of structured light reflected from AM surfaces after cropping for 3D characterization; (b) the entire reconstructed area which includes the rough AM surface (inner square); (c) the 3D view of only the AM surface (1-7 mm in (b)) derived from the reconstruction data from (b).

2.4 Conclusion and Discussion

A simple and robust digital phase-shifting Moiré technique is proposed for mapping and characterizing the 3D topography of metallic surfaces with micron scale features. The Moiré pattern results from the superposition of the reference structured light and the deformed pattern, and the desired phase difference map is calculated from spatial filtering of the Moiré patterns. A simple interferometric method is used to generate the sinusoidal fringes of varying spacings as the structured light which can provide horizontal resolutions in the order of tens to hundreds of microns. Use of the digital phase-shifting method allows for the generation of the reference patterns with desired phase shifts in high precision, thereby allowing for a single capture of the deformed pattern from the object surface, and significantly simplifies the experimental procedure. The feasibility of the method is shown by an example of the metallic screwhead. Application to mapping and roughness characterization of AM products has been explored.

Our preliminary results on AM products suggest that the proposed 3D MT still needs to be improved, which also indicates directions for future optimization. First, the design of the digital filter is key to obtain desired information from the deformed fringes. The optimal design of the digital filter for different surfaces is an interesting topic. Automated intelligent selection and design of digital filters, possibly based on deep learning, for different object surfaces based on their spectrum will be further investigated in the future. Another improvement is in the area of enhancing the resolution of the captured fringe pattern, this depends on our ability to generate and record denser fringes. The theoretical limit is fringe periods in the order of a few microns, but the optical setup to achieve this may be more challenging. Narrower fringes not only carry more information, but also enable more separation between zero-order and first order components in the spectrum, which can be beneficial for filtering. When the position of the first-order sideband is further away from the carrier, the mutual interference between the various components is expected to be less, and the signal-to-noise ratio of the reconstruction will therefore be higher. However,

the ability to capture denser fringes on the camera requires better resolving power or optical magnification of the deformed fringes, this will be further explored in the future. Optical methods to reduce speckle will also be investigated, viz., averaging over multiple captures, and compared to incoherent techniques.

In our method, the phase of the reference pattern is taken to be a constant rather than a position dependent variable, as would be the case if it were captured experimentally. In the case where the phase is position dependent, we speculate that the subtraction approach might reduce some effects of noise, and will be studied in the future.

CHAPTER III

APPLICATION OF STRUCTURED LIGHT TO 3D IMAGING OF PHASE OBJECTS

In this Chapter, the structured light method has been extended to the reconstruction of transparent phase objects. A simple non-interferometric incoherent ray propagation model is introduced to perform 3D profiling of transparent objects with typical thicknesses in the order of mm to cm by analyzing the distorted captured image behind the object. A 2D cosine fringe is used as the incident reference image, whose periodicity is markedly altered by the shape of the object. As a proof-of-principle, thick plano-convex blocks of glass are used as test phase objects. By monitoring the local change in the period, the surface profile is simulated and optimized to achieve minimal error with experimental data to determine the final morphology. The successful reconstruction of a bi-cylinder further demonstrates its feasibility for more complex applications. Our proposed method is simple, robust, straightforward, single-shot, and can be used with coherent or incoherent illumination. Moreover, the implementation of this technique on arbitrary transparent objects is theoretically feasible and promising.

3.1 Introduction

Over the past several decades, 3D imaging of reflective objects has matured and been commercialized as discussed before. However, reconstruction of transparent/translucent objects [80], important in machine vision, remain a challenge. In a broad sense, in addition to glass products like lenses, smoke [81], water surface [82,83], chemical gases, and biological tissue specimens [5], etc. can all be considered as transparent objects. Since the intensity of light passing through these objects is constant and only the refractive index of the material and its shape causes the optical path differences, they can be regarded as objects of uniform intensity and carrying phase information. Therefore, transparent objects like these are also called phase objects. Such objects may have complicated transmission and reflection mechanisms while interacting with light

rays, so the information in the captured images cannot be accurately located on the object. Moreover, due to the influences of the nature of materials and the surrounding environment on light propagation, it may be difficult to directly infer the 3D morphology of the target object from recorded images, which leads to the failure of traditional laser scanning and depth cameras to reconstruct phase objects effectively.

3.1.1 Existing Principal Methods

For the 3D measurement and reconstruction of transparent objects, current research mainly includes holographic interferometry [84], spectral confocal method [85], light-path triangulation [86-88], polarization imaging [89,90], shape from distortion method [91,92], reflection reconstruction method [82], scanning from heating [93], and tomography for fluids like smoke and flames [94]. Beyond these, physical or chemical intrusive methods are also an option [95]. Transparent objects can be sprayed with some developer to enhance the surface's reflective properties, then following the same procedure as reflective objects; however, this method is invasive. Alternatively, the object can be immersed in a solution with a uniform refractive index and reconstructed using tomography. In what follows, four of the non-invasive methods mentioned above are described in detail.

Holographic interferometry [84] uses a CCD to record the interference image generated by the reference laser light and another beam passing through the object, and then obtain 3D information using Fresnel diffraction, Fourier optics, and other related optical propagation theories. As an extension of the traditional single-wavelength holography, the dual-wavelength approach has also been developed. However, both can be limited by the small measurement range of objects' dimensions and high-resolution requirement of recording device. Also, the depth of field measured by holographic interferometry is quite small, thus the fringes will defocus for thick transparent objects [84]. In general, this technology is mainly used for weak phase objects such

as gas concentrations and the observation of tissue cells, and not for larger transparent objects with significant thickness.

Light-path triangulation method determines light rays passing through the transparent object via analyzing calibrated reference images at different positions or approximate estimation from optical flow data [96]. This technique can recover multiple real 3D coordinates for each pixel and then fit them into a light path from the object. Taking the work of Kutulakos and Steger [88] as an example, the correspondence relationship between the incident ray and the outgoing ray passing through the transparent object is first obtained. Then, the triangulation algorithm is applied to calculate the depth value corresponding to the incident ray passing through each pixel on the image plane. After that, the 3D morphology can be reconstructed. This method can yield the 3D point cloud and the corresponding normal vector information on the object surface simultaneously, but requires more than one camera to provide multiple positions or angles of view. Even so, multiple reflection/refraction and subsurface effects cannot be accounted for. In this technique, the calibration of each reference point at different propagation locations mainly depends on the algorithm. Accordingly, the quality of reconstruction results relies on the accuracy of the continuously optimized model.

Polarization imaging [89,90] is based on the Fresnel reflection equation to derive the mathematical relationship between the states and degrees of polarization and surface normals of the transparent object. Since natural light turns into partially polarized light after reflecting from, in this case, the transparent object, and the polarization state of outgoing light rays contains information about the object's shape, its morphology can be reconstructed via physical optics. This method is novel and relatively low-cost, because the light source can be an incandescent lamp. Nevertheless, the experimental set-up and procedures are involved. A linear polarizer is added and should be rotated many times to change the angle of polarization of the reflected light, and the CCD should take one picture after each rotation.

Moreover, the whole calculation is based on some assumptions that the refractive index of the object is known, and the surface is absolutely smooth, closed, and with no self-occluding regions. Polarization imaging has gained much attention in recent years. Since it can reveal information that pure-digital computer vision research cannot replace, this novel optical approach is promising [89].

Shape from distortion method has originated in the water surface imaging in 1990 [91]. A camera lens located at a plane perpendicular to the normal to the average water surface is used to capture a series of images of the target at the bottom of the tank being distorted by water fluctuations. The optical flow algorithm is utilized. The mean of the pixel tracks is approximated as the average water surface, thus producing the desired undistorted image. Morris and Kutulakos have since optimized this technique [92], but it is still limited to underwater image reconstruction.

Among the other techniques, the spectral confocal method [85] only makes single-point measurements each time, resulting in extremely low efficiency. Although the reflection reconstruction method [82] can rebuild complex transparent objects even with different internal materials, it requires an extremely high precision data acquisition system and complicated data recording operation. Besides, the infrared based scanning from heating proposed by Goneneren *et al.* uses laser heating and thermal imaging principles [93], which is quite different from other approaches.

3.1.2 Structured Light

Similar to the initial idea of the light-path triangulation, tracing the light path to acquire the phase information carried by each pixel is our objective. However, simplifying the experimental set-up, especially cameras, and streamlining operations are prerequisite for applications. According to our description in Chapter II, a single-shot structured light method has been used for reconstruction of reflective objects, and it is now extended to transparent objects. Thus, it is our

objective to use structured light to illuminate transparent objects for one capture and use simple ray tracing to deduce the shape of the phase object.

Based on previous research, the 2D cosine fringe has been chosen as the structure of the light source, also known as the reference image. Because our transparent objects to be characterized have larger size (typically in the order of a few cm), and because using a laser to derive the interference fringes for use as structured light may produce strong directed reflection on smooth glass surfaces and then form flares on the CCD at certain angles, a traditional projector illumination has been employed. Unlike the case of the reflected pattern from a surface where Eqs. (2-8) and (2-9) can be used to determine the morphology or height profile from the phase, there is no one-to-one correspondence between the pixels on the recorded deformed image and the actual locations on the object's surface, due to refraction of light through the sample. Hence the information of the phase shift carried by the captured image as in the case of the reflected structured light cannot be directly converted to height/depth map. In this case of the transparent object, the variation in the period of the deformed cosine intensity pattern transmitted through the object provides information of its thickness or phase. One can view the information that is modulating the carrier as the phase information of the object. By analyzing the carrier frequency, the morphology of the target can be determined through a process of optimization, as discussed below.

3.1.3 Inverse Ray Tracing

The principle of forward ray-tracing is to trace each incident ray interacting with the target and then intersecting with the camera's image plane to obtain the color and brightness of each pixel, given the 3D geometry and material properties of the object. Inverse ray-tracing is the opposite procedure of inferring the target's shape from the collected images [ref]. In general, a reasonably hypothetical 3D model is first used for forward ray-tracing, and then the generated deformed image is compared with the experimental image, and the 3D model is continuously optimized for

reconstruction. Inverse ray-tracing is not a commonly used approach for phase reconstruction, but is generally considered in certain methods, as described below.

The level set method, introduced by Osher and Sethian [97,98], for computing the solution to fluid-interface problems is the most typical technique that comes closest to the inverse ray method. It is a computational technique that relies on an implicit formulation of the interface, represented through a time-dependent initial-value partial differential equation. The equation of motion of the interface is numerically approximated based on conservation laws. Typical applications are in fluid mechanics, bubble dynamics, ship hydrodynamics, and inkjet-printhead design. In the field of computer vision, Goldlucke *et al*. [99] have implemented residual optimization as a minimization problem for an energy functional. These work focus on solving a large number of mathematical calculations, so the theories and models are complex. Besides, use of polarization properties of light [100], use of chemical fluorescent materials [101], etc. to inversely trace rays have been proposed.

As stated earlier, the principle of inverse ray-tracing is incorporated into our structured light method, which is continuously simulating the forward propagation of the designed cosine illumination and gradually optimizing the shape of the transparent object. Specifically, several different surfaces have been digitally generated to simulate a set of deformed patterns. Next, the spatial variation of the cosine period has been used as the criterion for the accuracy of the reconstruction through comparison of the simulation and the experiment. When the numerical results and the experimental data are identical, the test object surface can be finally identified. In a more general sense, any structured light that is encoded with the phase information can be used for comparing simulation results with experimental observations with the aim of reducing the difference and thereby optimizing the target morphology.

3.1.4 Organization of the Chapter

In this Section, we have described the background and various methods of transparent object reconstruction in detail. A combination of structured light and inverse ray-tracing have been reviewed. Section 3.2 illustrates the theoretical calculation and some simulations. In Section 3.3, three transparent objects have been successfully reconstructed in our experiments. Rigorous error analysis is demonstrated to determine the results. Our proposed set-up and operation are simple and straightforward, and lends itself to fast computations of the surface morphology. The feasibility of this method for more complicated morphologies has been discussed in Section 3.4.

3.2 Theory and Simulation

3.2.1 Ray Propagation Model

Based on Snell's laws of light refraction, the light path through the transparent object can be computed. Figure 3-1 illustrates a top view of parallel rays passing through a transparent object. In this figure, the object surface with which the light first interacts is considered to be perpendicular to the direction of incident rays. Therefore, the propagation direction of incident light rays does not change at this interface.

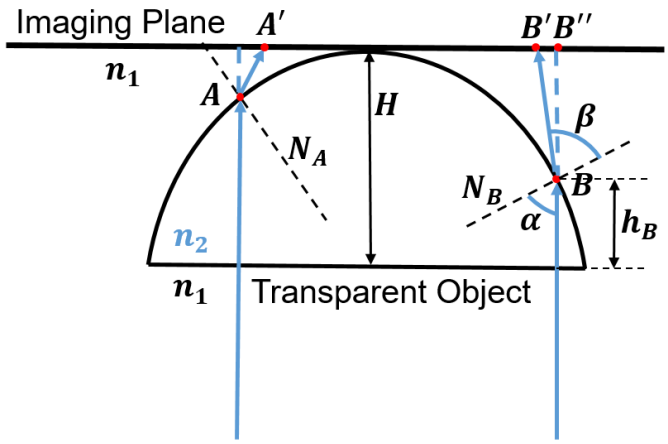

Figure 3-1: A top view of parallel light rays passing through a transparent object.

Next, the light travels through the interior of the transparent object with the refractive index of n_2, and then interacts with the second surface. Because the curvature of the surface is different at different locations, the normals have different directions, as indicated by the two dashed black lines N_A and N_B passing through points A and point B, respectively. Points A and B represent the intersection of two different parallel rays and the second surface of the object. Since the directions of normals are different, the magnitudes of the incident angles at those points are also different.

The transparent object is assumed to be surrounded by air, hence its refractive index n_1 can be regarded as 1. The refractive index of glass is approximately $n_2 \approx 1.5 > n_1$ Therefore, at the second surface of the object, when the incident angle α is less than the critical angle θ_c, the rays are refracted, but when α is greater than θ_c, the rays are totally reflected and cannot be recorded on the imaging plane.

The blue rays show the light paths after refraction. Points A' and B' represent the intersections of the refracted rays and the imaging plane. The imaging plane is assumed to be placed very close to the object's curved surface at a distance H from the flat surface of the object. h_B indicates the height information of point B, that is, the distance from point B to the object's flat surface. B'' represents the position on the imaging plane where the light passing through B would have been if there were no object. β is the angle of refraction in the air. Triangle $BB'B''$ is enlarged and shown in Figure 3-2.

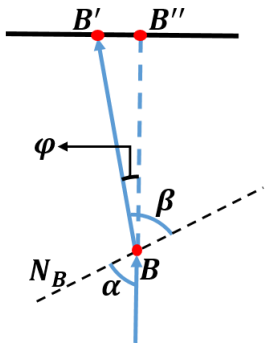

Figure 3-2: The enlarged view of triangle $BB'B''$ shown in Figure 3-1.

From Figure 3-2,

$$\beta = \alpha + \varphi, \tag{3-1}$$

$$tan(\varphi) = \frac{B'B''}{BB''}. \tag{3-2}$$

Now, from Figure 3-1,

$$BB'' = H - h_B. \tag{3-3}$$

Also using Snell's law,

$$n_2 \times sin(\alpha) = n_1 \times sin(\beta), \tag{3-4}$$

where n_1 is assumed as 1. Combining Eqs. (3.1) - (3-4), the length $B'B''$ can be derived:

$$B'B'' = (H - h_B) \times tan\left[arcsin\left(n_2 sin(\alpha)\right) - \alpha\right]. \tag{3-5}$$

It can be seen from Eq. (3-5) that the distance $B'B''$ is related to the object thickness and the nature of the surface where the ray is refracted (which determines the angle α). Since the light incident at point B is recorded on the imaging plane at B', the light intensity information originally at point B'' without the object is changed to point B' due to the presence of the object. The lateral displacement of the incident structured light in the deformed transmitted pattern can thus be calculated, using Eq. (3-5). It is assumed that any light that is totally internally reflected within the transparent object suffers multiple reflections and is lost, and thus does not contribute to the transmitted light pattern.

3.2.3 Cosine Pattern Simulation

To derive the morphology of the transparent object from the deformation of the incident structured light, different objects with curved surfaces of various radii of curvature have been digitally generated and then put into the ray propagation model derived in the last sub-section.

Taking one simulation as an example, a reference fringe is shown in Figure 3-3(a), the generated surface of the transparent object is shown in Figure 3-3(b), and the deformed cosine pattern calculated by the model is shown in Figure 3-3(c). A cross-sectional cut of the Figure 3-3(c) is plotted in Figure 3-3(d). showing the intensity variation as a function of space. Typical dimensions of the pixel can be tens of microns, and will be made more precise later.

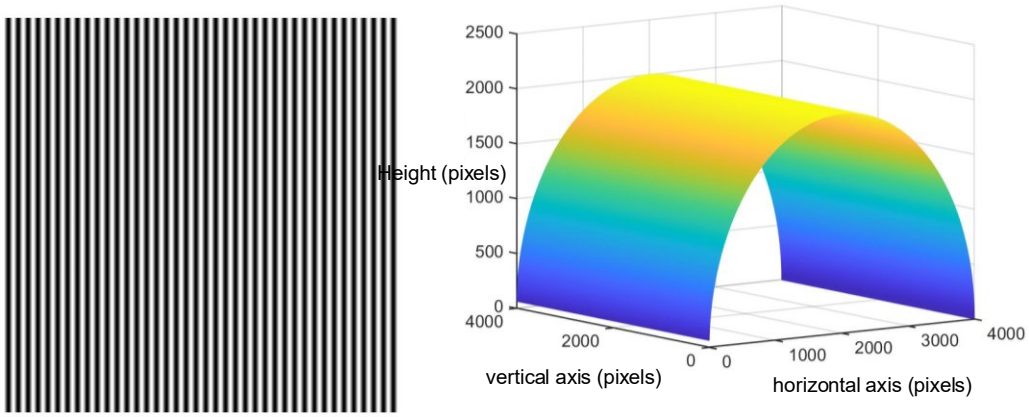

(a) (b)

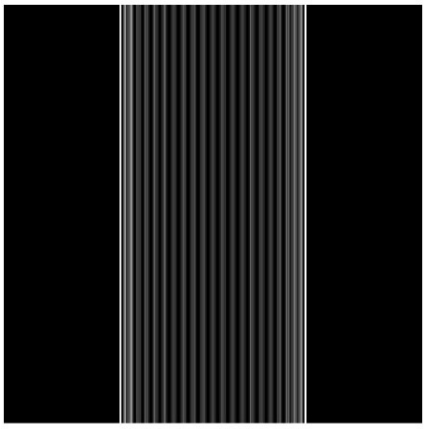

(c)

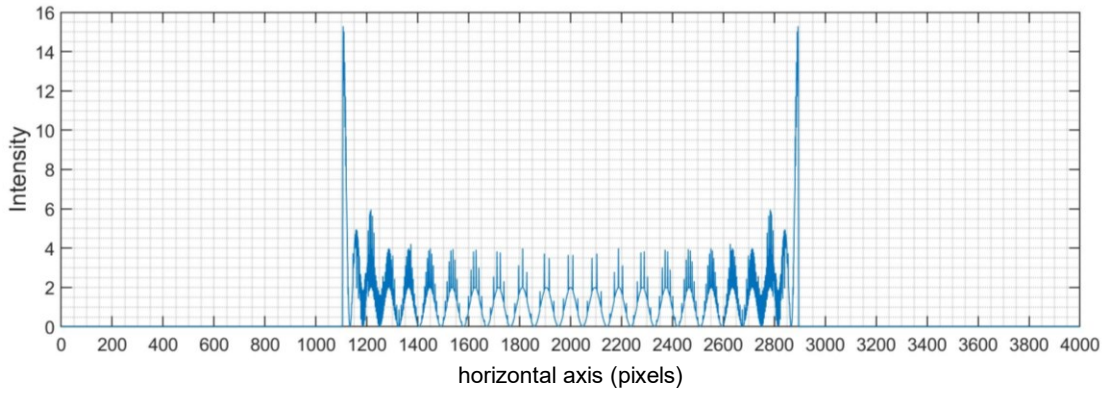

(d)

Figure 3-3: The illustration for cosine-type pattern passing through a simulated transparent object: (a) 2D vertical cosine pattern as the reference image; (b) one simulated transparent object; (c) the calculated deformed image; (d) an arbitrary horizontally extracted line from (c). Typical pixel dimension is tens of microns.

In this case, the reference image for the structured light is a $4000\ pixels \times 4000\ pixels$ size cosine fringe with a period of $100\ pixels$, which is produced by the expression:

$$I_{ref}(x,y) = 1 + cos(\frac{2\pi x}{100}), \tag{3-6}$$

where I_{ref} for the intensity values is shown as the brightness in Figure 3-3(a). The corresponding digitally produced surface of the transparent object has the same size, which is a semi-circular cylinder whose height is given by

$$h_{obj}(x,y) = \sqrt{H^2 - (x-H)^2}, \tag{3-7}$$

where h_{obj} represents the height of each point on the surface (similar to h_B for point B in Eq. (3-5)) , and H is the maximum height value, which is the same in Figure 3-3. Since the cylinder has a semi-circular cross-section, H can be regarded as the radius here. Note that $H_{obj} = 0$ at $x = 0, 2H$, as also seen from Figure 3-3.

According to the theory, the deformed image, generated by passing the structured light pattern in Figure 3-3(a) passing through the object shown in Figure 3-3(b), is shown in Figure 3-3(c). The brighter regions represent higher intensity. It is to be noted that there are large black areas on both

sides of the figure, which is consistent with the effect of total internal reflection, causing the loss of light transmitted through the object. Since Figure 3-4(c) is uniform along the vertical direction, any horizontal cut can be used to observe the deformation of the cosine pattern as shown in Figure 3-3(d). The horizontal axis here is the same as in Figure 3-3(b), and both are in pixels. The y-axis indicates the intensity values of the deformed cosine fringe.

As our experimental objects are glass products, n_2 of the ray propagation model has also been set to 1.5 in the simulation. Using Eqs. (3-5) and (3-7), the distorted pattern can be found and plotted as in Figure 3-3(c), by determining the value of α of each pixel. Obtaining α requires the Surfnorm function in MATLAB to determine the orientation of the normals. Figure 3-4(a) below demonstrates the cross-section of the surface in Figure 3-3(b), with the normal at each pixel shown in red. The normals are all pointing out from the surface. For a clearer view, the horizontal pixel interval from 1950 to 2050 has been enlarged and shown in Figure 3-4(b).

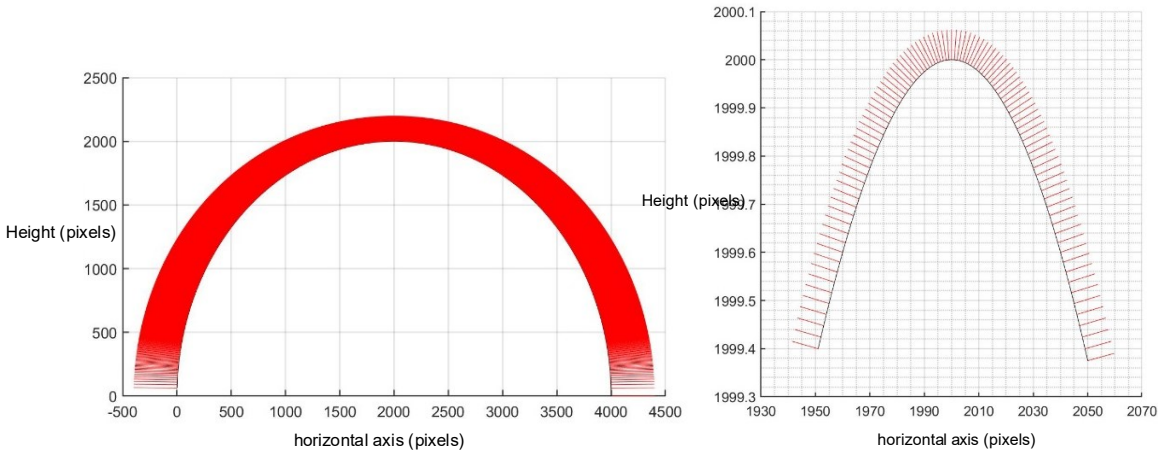

(a) (b)

Figure 3-4: The cross-section of the simulated surface with normal lines: (a) for the whole surface; (b) for the enlarged horizontal pixel interval from 1950 to 2050. Typical pixel dimension is tens of microns.

To explore the effect of distortion during ray passage through a transparent object, the same process has been applied to different digitally generated objects. Following the semi-circular

cylinder simulations above, cylinders described by ellipses for the surfaces with different ellipticities e have been considered. Their shapes are given by

$$h_{obj}(x,y) = \sqrt{H^2 - ((x-H)/e)^2}. \tag{3-8}$$

Elliptic cylinders with varied ellipticity parameters have been produced, as shown in Figures 3-5 below. Note that $e = 1$ describes the circular shape, which was considered earlier.

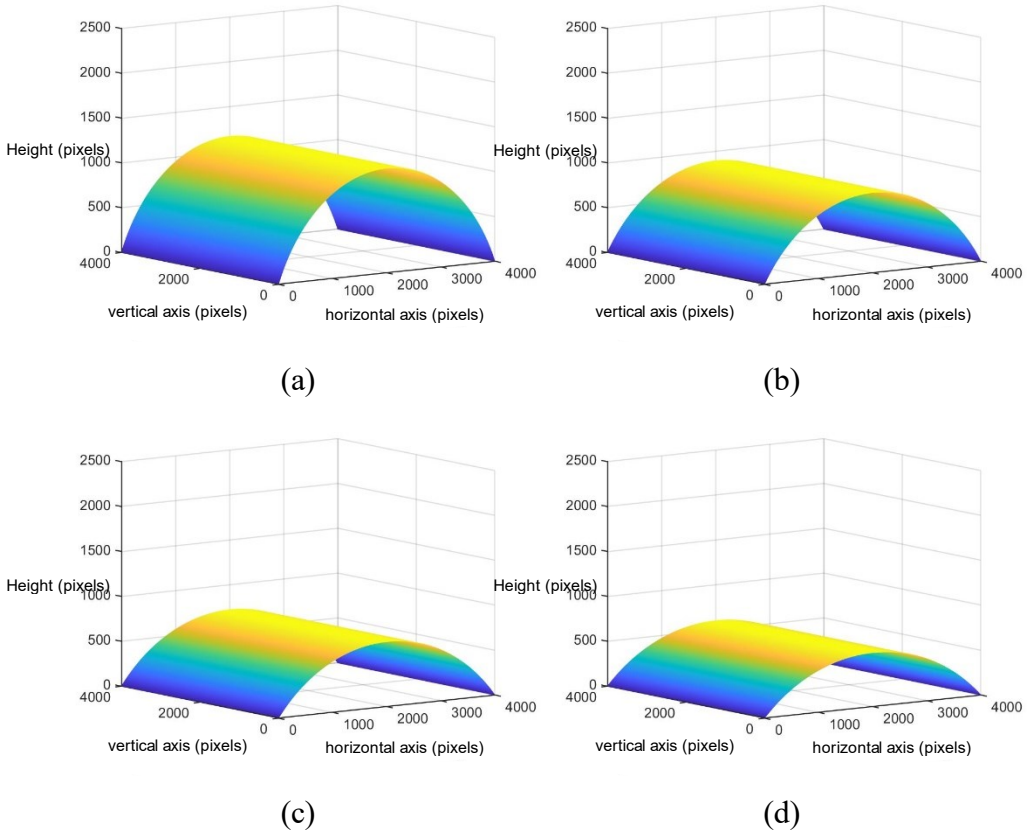

Figure 3-5: Four elliptic cylinders with varied ellipticities: (a) $e = 1.1$; (b) $e = 1.2$; (c) $e = 1.3$; (d) $e = 1.4$. Typical pixel dimension is tens of microns.

Note that the lowest points of each cylindroid's surface have been shifted to the zero planes, which means that this whole surface has been subtracted by the minimum height value for visual comparison. Besides, the range of the z-axis has also been set to be the same as the circular cylinder in Figure 3-4(b). Based on the identical zero starting height, the different maximum heights shown above can verify the difference of ellipticities.

Using the identical cosine fringe shown in Figure 3-3(a) as the reference image, the four object surfaces in Figure 3-5 show the deformed images as in Figure 3-6, and their deformed images have been derived using the ray propagation model, respectively. As before, a cross-sectional cut of the images yields the intensity variation as a function of space, similar to Figure 3-4(d). Note that the dark regions on each side diminish with increased ellipticity, indicating reduced total internal reflection.

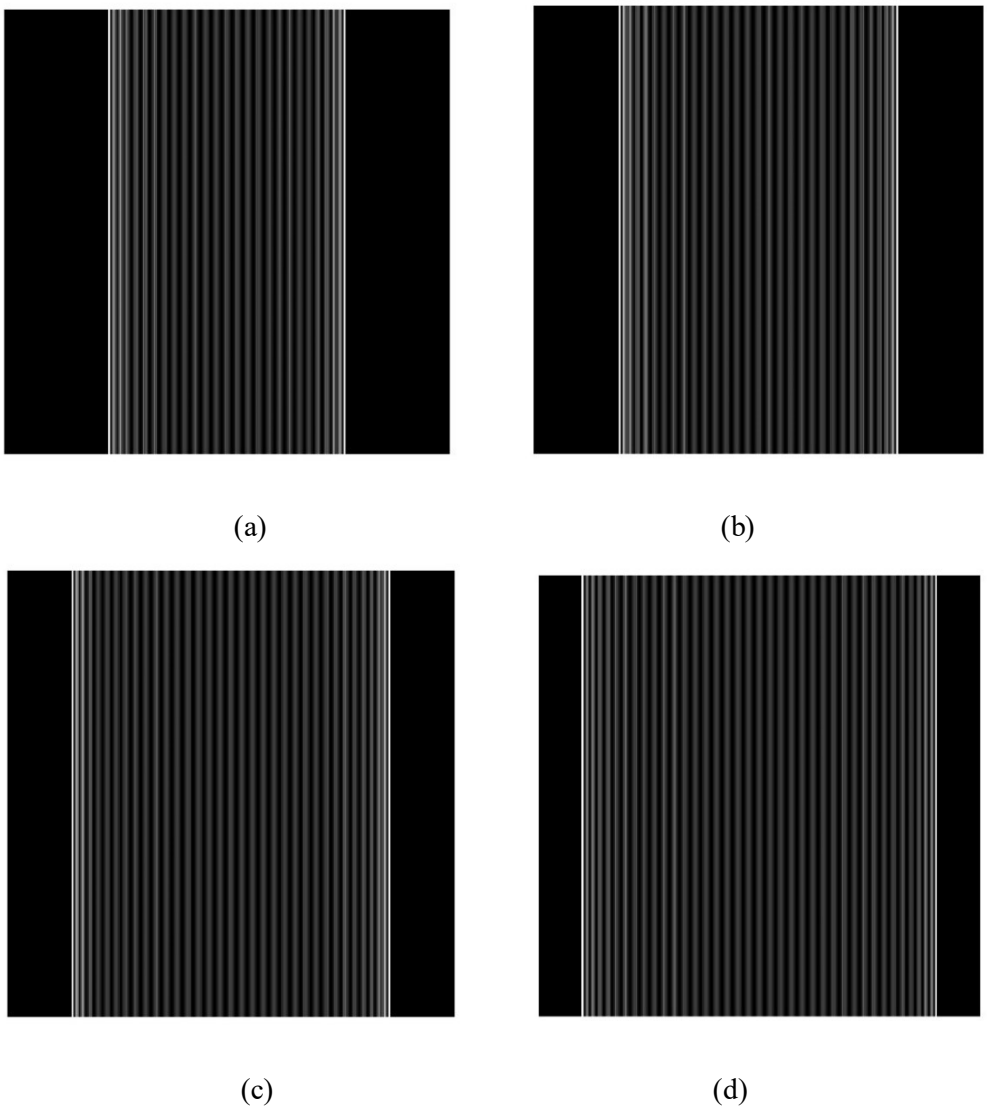

Figure 3-6: Four deformed cosine pattern images derived from the four surfaces in Figure 3-5. (a) $e = 1.1$; (b) $e = 1.2$; (c) $e = 1.3$; (d) $e = 1.4$.

The period information of these deformed cosine patterns has been studied in more detail. From each intensity plot showing its spatial variation, the minima have been located to calculate the period of each peak (in pixels). The variation of the periods with space ($x - axis$) of the five deformed patterns with eccentricities $e = 1.0, 1.1, 1.2, 1.3, 1.4$ are plotted in Figure 3-7. As expected, the periods decrease with increasing distance from the center of the graphs. The trend is consistent with the shape of the surface cross-sections.

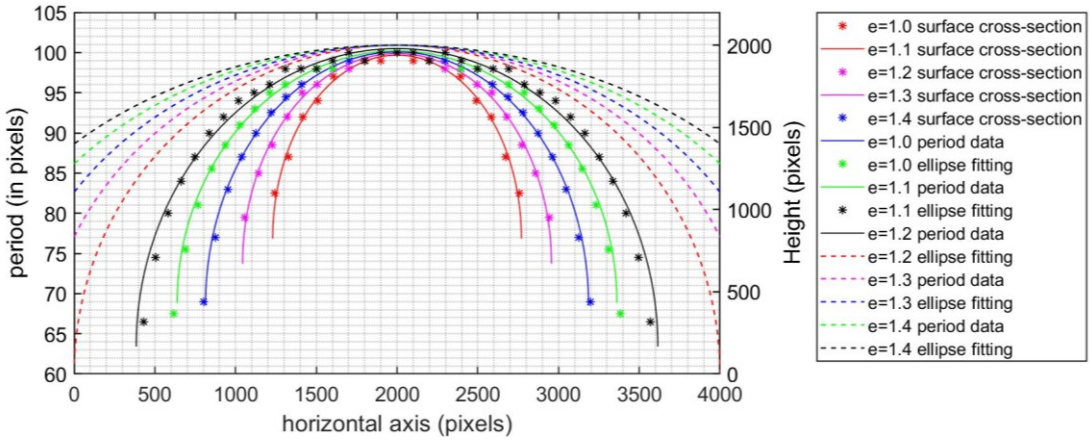

Figure 3-7: The fitting curves of cosine period data and the elliptical surface cross-section shapes. The asterisks represent the cosine period data. The solid lines represent the fitting ellipses of these data based on the least square method. The dash lines represent the cross-section curves of simulated objects. Different colors indicate different ellipticities of simulated objects, as shown in the legend on the right. Typical pixel dimension is tens of microns.

The dots in the figure above indicate the actual data and the dots are connected by a fitting algorithm based on the least squared method [102] for the sake of comparison. When $e = 1.0$, Eq. (3-8) reduces to Eq. (3-7), which means that the cylinder's cross-section has been changed from a semi-ellipse to a semi-circle. It can be seen that these curves decrease less rapidly as the ellipticity increases, and this flattening of the profile appears to be in consonance with the increase in ellipticities. It is also clear that the period and surface height have an obvious positive correlation.

3.2.4 Discussion of Simulations

As long as a one-to-one correspondence between the shapes of the refracting surface and the fitting cosine period number curves exists, the object's morphology can be derived from the deformed pattern image. A simple relationship is, however, hard to find due to the complicated nonlinear relationship between the period and the curvature (or eccentricity). For instance, based on Figure 3-7, we have attempted to find a polynomial fitting curve relating the period to the height, as shown in Figure 3-8 for the case of $e = 1.0$. Although there is a reasonable fit over a range of heights, the fitting degrades for smaller values of the period. Other standard fitting functions have been tried; more on this will be pursued in the future.

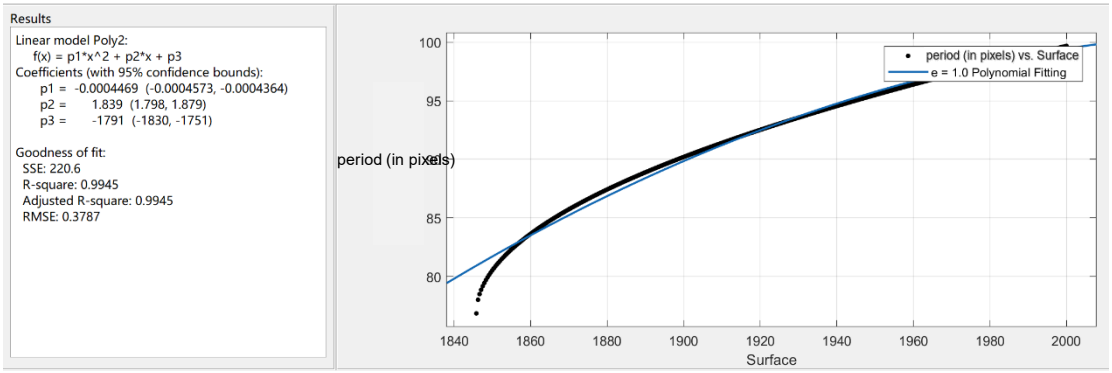

Figure 3-8: The fitting results of the original surface cross-section shape and the fitted ellipse expression of cosine period data in $e = 1.0$ condition, via digital fitting method using a quadratic polynomial. Typical pixel dimension is tens of microns.

3.3 Experimental Setup and Results

3.3.1 Experimental Setup

In order to record the deformed image after the transparent object, the simple experimental set-up shown in Figure 3-9 is used. The Optoma EX536 Projector is capable of displaying 2800 Lumens at its brightest setting with a native resolution of 1024×768. The computer has connected to the projector to project the cosine fringe image onto the object's surface. In reality, the object's size can be much smaller than the projected area of illumination. A camera (iPhone

12 Pro 4000×3000 pixels or Canon 800D 6000×4000 pixels) is focused on a plane immediately behind the object (referred to as the imaging plane) and indicated by a dashed line to record the deformed pattern. The blue rays indicate the direction of propagation of the light – it is assumed that the light pattern is nonspreading. The camera is first focused on a spot on a white sheet of paper located immediately behind the object. The paper is then removed and with the camera setting unchanged, the deformed intensity pattern is recorded. Since our theory pertains to light rays as they exit the surface, the intensity pattern is monitored immediately behind the object.

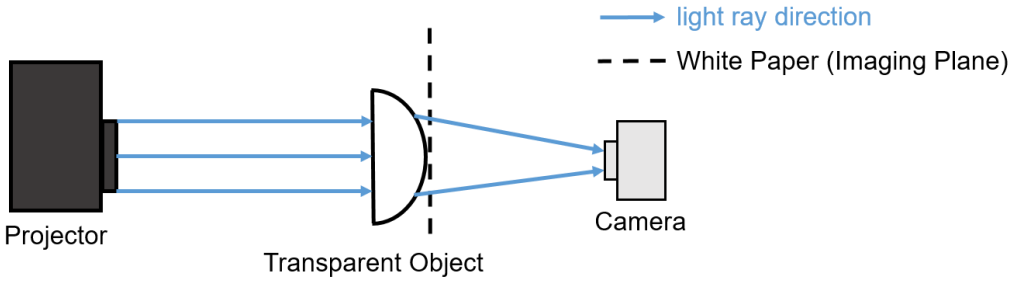

Figure 3-9: The top view of the experimental set-up.

Since the projected white light is actually made up of various light colors changing rapidly in time (less than 0.1 seconds, which is the persistence of the eye), the camera's shutter time must be longer than the one cycle of all colors. Otherwise, the resulting image may appear in some mixed colors instead of white. The camera aperture has been set to a small value to prevent overexposure due to the slightly longer shutter time. It was found that for a f-number $f\# = 22$, photos taken with the automatic shutter look purely black and white.

3.3.2 Transparent Semi-circular Cylinder Reconstruction

The first experiment conducted was on a transparent object which is a half-cylinder made up of two surfaces, one flat and one curved, as shown in Figure 3-10(a) below. The target object has been positioned as shown in Figure 3-9. The light from the projector first interacts with the flat

surface, passes through the glass material's interior, and next interacts with the second curved surface. Finally, the deformed pattern is imaged on a white paper positioned as shown in Figure 3-9, and recorded by the camera.

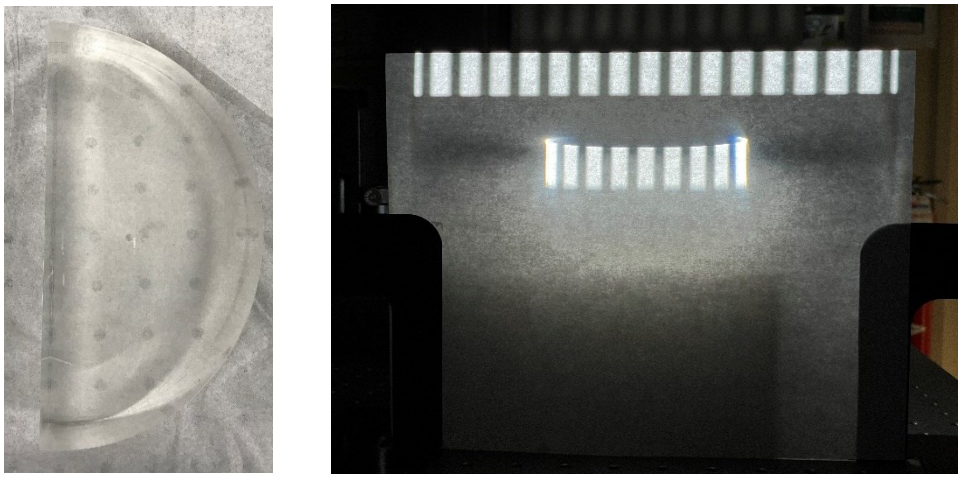

(a) (b)

Figure 3-10: The illustration of the first experimental object. (a) the transparent half-cylinder object with one flat surface and one undetermined curved surface; (b). the recorded deformed image on the white paper, along with the undeformed image.

Since the glass cylinder is only 5-centimeter-high, only part of the projected image enters the transparent object. Thus, the upper pattern area in Figure 3-10(b) is an undeformed reference fringe in the imaging plane, while the deformed image is the lower pattern. In this case, the deformed image and the reference pattern distributed in different areas of this photo could be obtained simultaneously in a single shot.

For data processing, a horizontal cut across the deformed pattern and the reference pattern is used to acquire the cosine distribution of intensity information, respectively. The enlarged deformed pattern along with the location of a horizontal cut (indicated in red), is shown in Figure 3-11(a); the corresponding intensity plot is shown in Figure 3-11 (b). Similarly, the intensity distribution of a similar horizontal cut from the reference pattern is shown in Figure 3-11 (c).

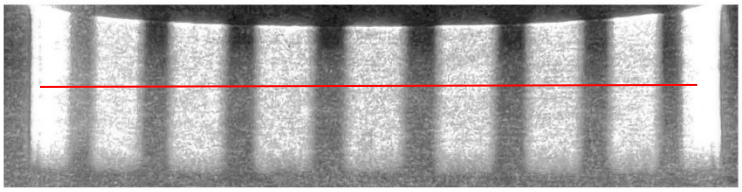

(a)

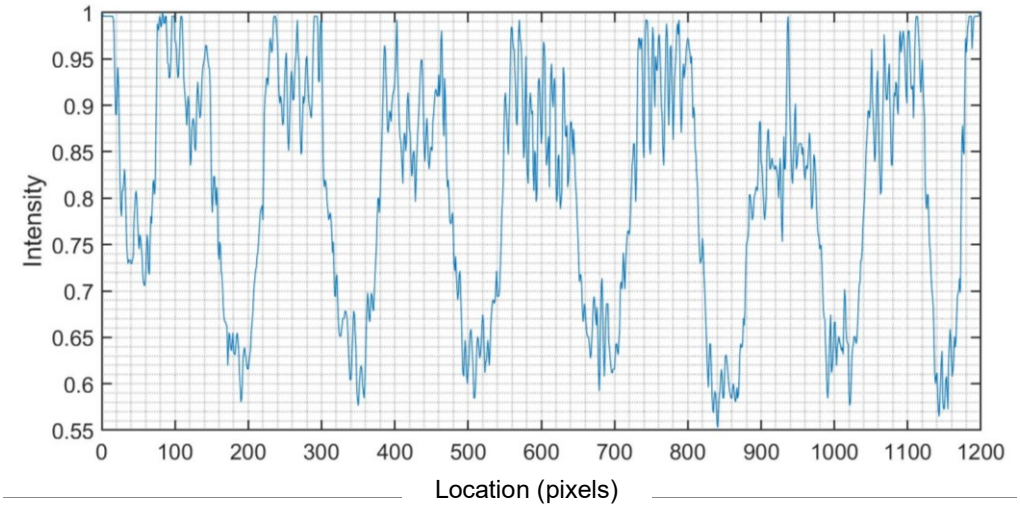

(b)

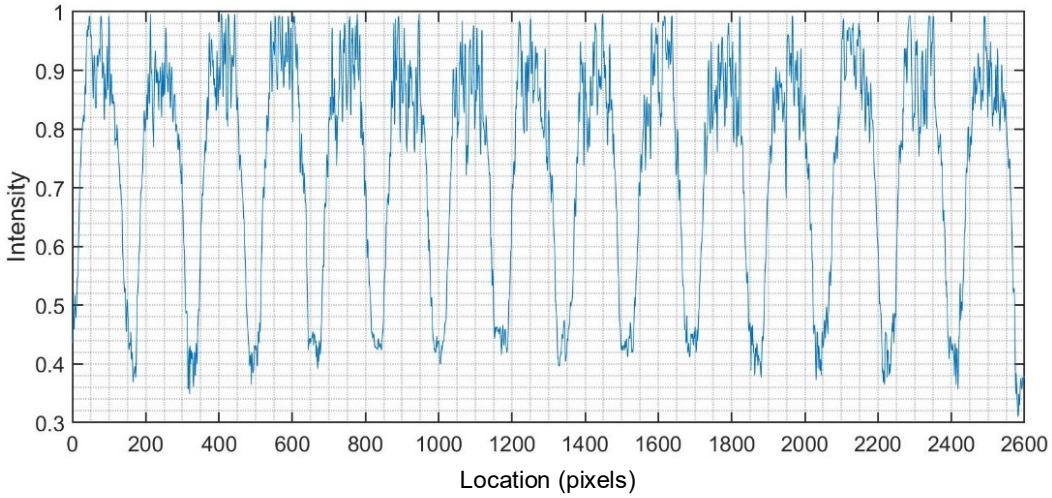

(c)

Figure 3-11: The intensity distribution of deformed image and reference patterns. (a) The intercepted deformed image area; (b) The intensity distribution extracted from one horizontal line, shown in red in (a); (c) The intensity distribution similarly extracted from a horizontal line from the reference pattern.

Locations of the valleys can provide information about the instantaneous periods. To overcome the effect of noise in these patterns, possibly from light scattering on the paper, points on the left

and right sides of the valley with the same intensity value have been found, and then the valley position has been calculated from the average of these two points. Taking the valley at around $190\ pixels$ as an example, two nearest points of approximate $Intensity = 0.67$ have been found on either side of it. Their locations are $165\ pixels$ for $Intensity = 0.6732$ and $205\ pixels$ for $Intensity = 0.6745$. Therefore, the valley's location can be identified as $185\ pixels$. Using this approach, the locations of the other valleys have been determined and are shown in Table 3-1. The instantaneous period can be computed by subtracting the positions of adjacent valleys. The position of the peak has been set at the mean of the locations of two adjacent valleys and is referred to as the central location in the table.

Table 3-1: Data processing for the first experimental transparent object

Valley Location (Pixel #)	Period (in pixels)	Central Location (Pixel #)	Translated Central Location (Pixel #)
52			
185	133	118.5	-478.5
344	159	264.5	-332.5
511.5	167.5	427.75	-169.25
683	171.5	597.25	0.25
850.5	167.5	766.75	169.75
1009	158.5	929.75	332.75
1142	133	1075.5	478.5

The translated center in the above table is derived from the third column of the data after translation. The purpose of this step is to have the deformed pattern's center at $x = 0$, thus eliminating the influence of different initial positions of the extracted red line. In this way, the two edges must appear at equal and opposite on the $x - axis$. In this case, the center appears at $(118.5 + 1075.5)/2 = 597$; thus, data in the third column are subtracted by 597 to get the

corresponding values in the fourth column. The instantaneous period (in pixels) has been plotted as a function of its translated center location in Figure 3-12. The red asterisks in the figure indicate the data from Table 3-1, and the solid black curve joining the points has been drawn using the spline function in MATLAB.

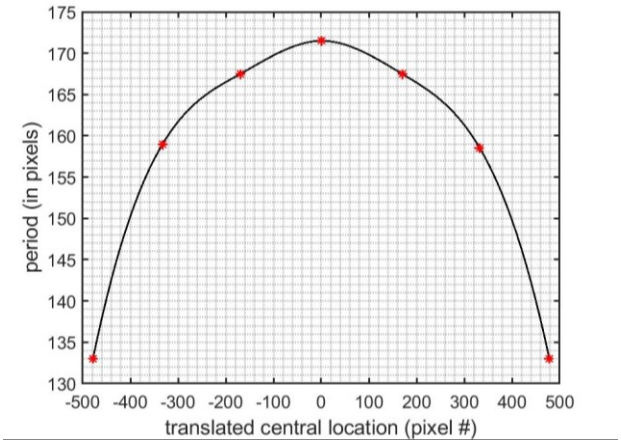

Figure 3-12: Instantaneous period (in pixels) as a function of its location.

Now, from Figure 3-11 (c), the period of the reference pattern can be estimated as $173\ pixels$. In the experiment, the actual physical length of a ten-period cosine reference fringe has been measured to be $144.2\ mm$. Thus, the spatial resolution for these recorded image(s) can be calculated as:

$$\frac{144.2\ mm/10}{173\ pixel} \approx 83.35\ \mu m/pixel. \tag{3-12}$$

Since the horizontal width of the object's flat surface has been measured as $20\ cm$, the pixel numbers occupied by the incident plane has been calculated to be 2399.45, which is approximated to $2400\ pixels$. In other experiments to follow with a similar setup, the pixels occupied by the incident plane's horizontal width can be read directly from the picture taken.

The height of the cylinder, i.e. the vertical length of the incident plane, has been measured as $5\ cm$. On the basis of Eq. (3-12), the reference image has a $y-axis$ height of $600\ pixels$ approximately.

The cosinusoidal reference pattern is shown in Figure 3-13 (a). It has a period of $173\ pixels$ and a size of $600\ pixels \times 2400\ pixels$. Next, cylinders with different shapes (i.e., eccentricities) have been digitally produced, as shown in Figures 3-13 (b-e) and then used to compute the outputs, namely the deformed pattern image, via the ray propagation model. This work is almost identical to the simulation process in Section 3.2.3, except for the size of the reference image and the generated surfaces. Elliptic (which includes circular) cylinders have been first considered.

(a)

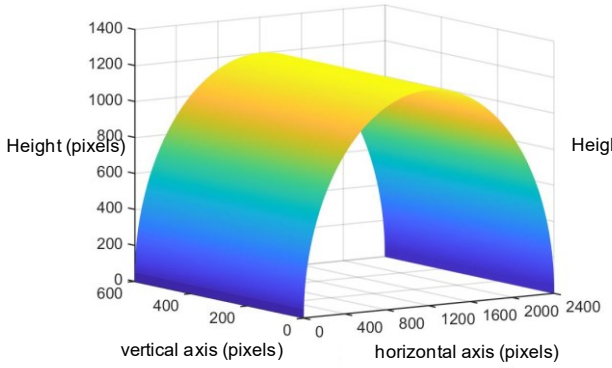

(b)

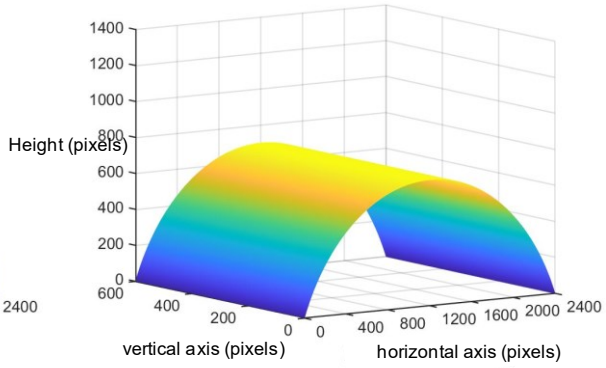

(c)

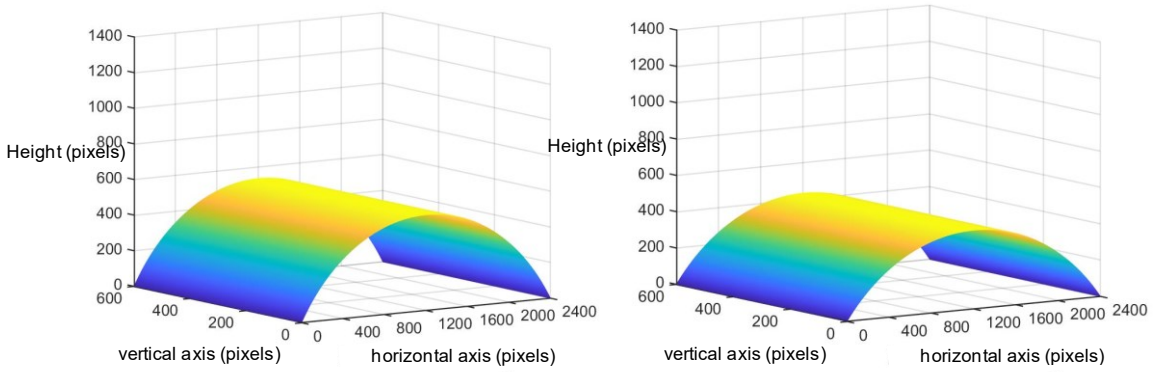

(d) (e)

Figure 3-13: The illustration of the digitally generated reference image (a) and four semi-elliptic cylinder surfaces with varied ellipticities: (b) $e = 1.0$; (c) $e = 1.1$; (d) $e = 1.2$; (e) $e = 1.3$. The axes ranges are derived from the experimental data. One pixel represents about 80 microns.

The refractive index of the material (glass) has been assumed as 1.5. The deformed patterns resulting from the four surfaces in Figures 3-13(b-e) above are shown in Figures 3-14 (a-d) below in sequence. An arbitrary horizontal line in these deformed images has been extracted one by one, and the light intensity - horizontal location curves have been plotted, as shown in Figures 3-14 (e-h).

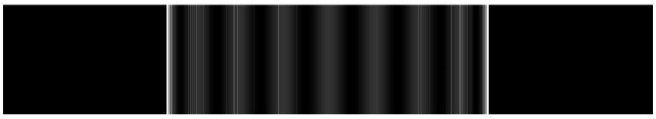

(a)

(b)

(c)

(d)

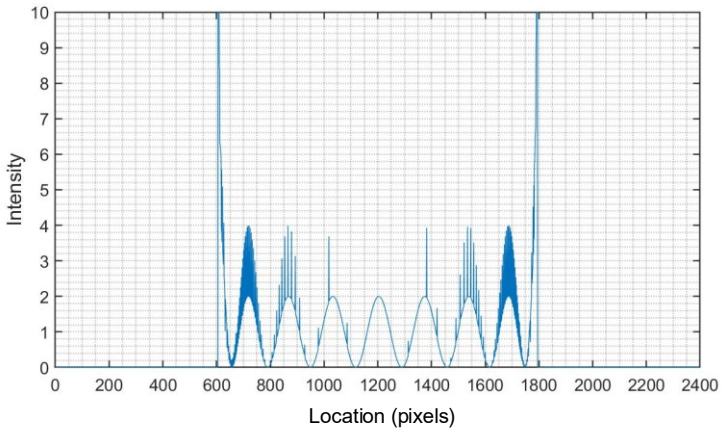
Intensity
Location (pixels)
0
1
2
3
4
5
6
7
8
9
10
0
200
400
600
800
1000
1200
1400
1600
1800
2000
2200
2400

(e)

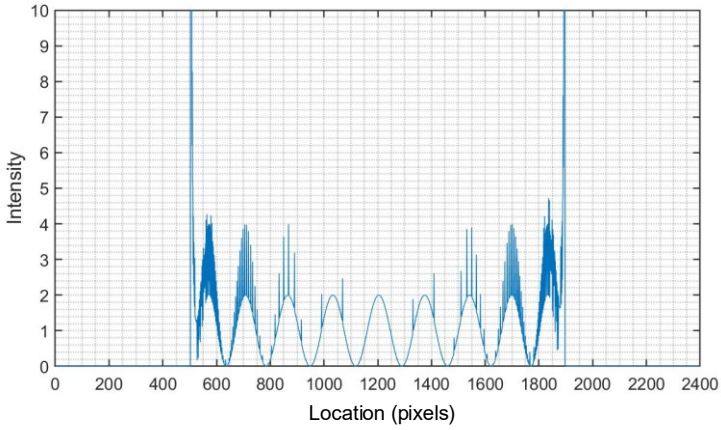
Intensity
Location (pixels)
0
1
2
3
4
5
6
7
8
9
10
0
200
400
600
800
1000
1200
1400
1600
1800
2000
2200
2400

(f)

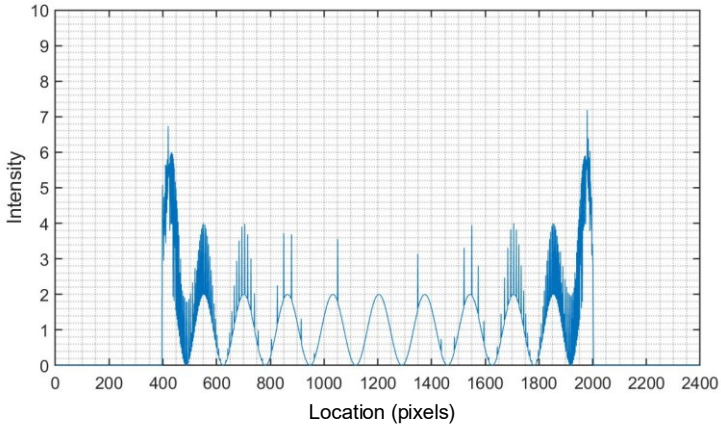
Intensity
Location (pixels)
0
1
2
3
4
5
6
7
8
9
10
0
200
400
600
800
1000
1200
1400
1600
1800
2000
2200
2400

(g)

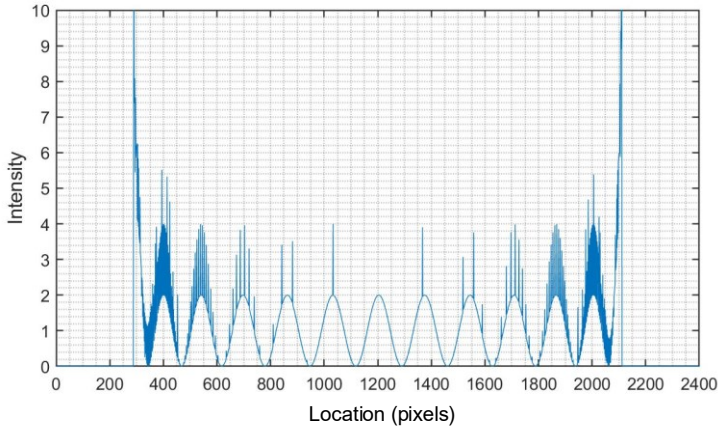

(h)

Figure 3-14: The illustration of the results of the light propagation model. (a-d). The deformed patterns resulting from the four surfaces in Figures 3-13(b-e); (e-h). The corresponding intensity curves of the extracted horizontal lines from (a-d). One pixel represents about 80 microns.

Similar to our earlier simulations, as in Figure 3-7, the valleys of the deformed cosine patterns in Figures 3-14 (e-h) have been found. The varying period numbers and the horizontal location of each peak center have been calculated. Finally, four tables similar to Table 3-1 have been derived for different ellipticities. From these data, the cosine period number vs. peak central location curves are plotted in Figure 3-15, along with the experimental results from Figure 3-12. To keep the horizontal position consistent, all of these central locations have been translated, just like before. It is noted that with the increase of the ellipticity parameter, variation of the period becomes flatter with increasing ellipticity, which is the same as the earlier conclusion.

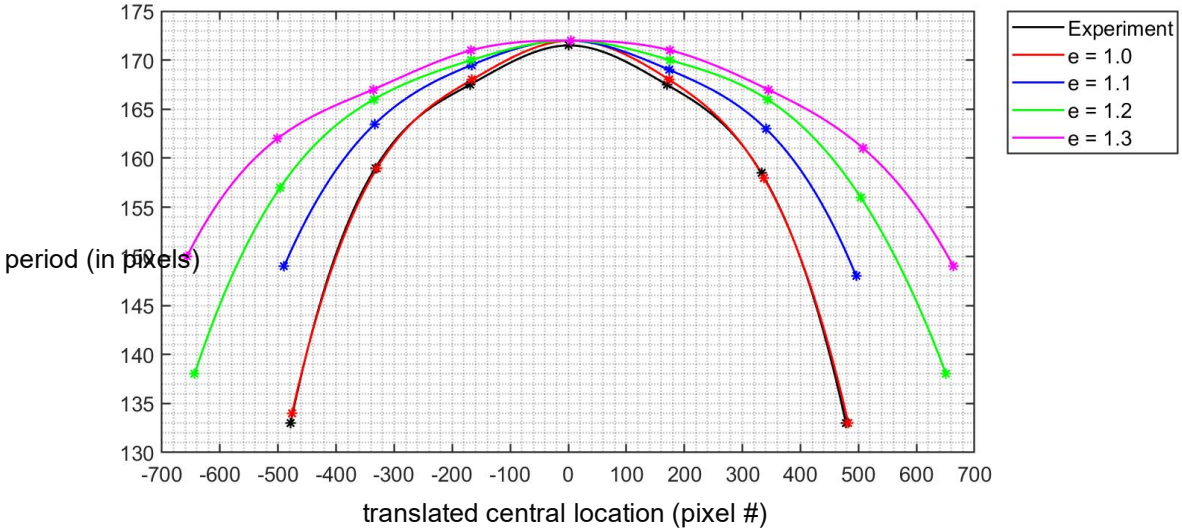

Figure 3-15: Cosine periods in pixels vs. peak central location data for the experiment and above four surfaces with different ellipticities. Different colors indicate different ellipticities of objects, as shown in the top-right label. One pixel represents about 80 microns.

It is evident from Figure 3-15 that the computed curve with $e = 1$ shows the best agreement with the experimental data. Seven cosine fringe periods with varying periods appear in the middle area of the deformed image, both in experiment and in theory. With increase in ellipticity, more cosine fringe periods are observed, as expected.

For more rigorous comparison, data from each simulated curve has been used to calculate the error when comparing with experimental values. However, values of the periods for the simulation results need to be computed at the exact translated central locations where experimental data have been plotted (see, for instance, the slight discrepancy between the abcissae of the central locations of the experimental (black) and simulated (red) curves in Figure 3-15). This "fitting" is done using cubic interpolation/extrapolation. The results are summarized in Table 3-2, which lists the "fitted" period from the simulation results at the exact translated central locations from the experiment.

Table 3-2: The fitted period number data via cubic interpolation method according to the experimental peak central location

Expt'l Central Location (pixel #)	$e = 1.0$ Fitted Period (in pixels)	$e = 1.1$ Fitted Period (in pixels)	$e = 1.2$ Fitted Period (in pixels)	$e = 1.3$ Fitted Period (in pixels)
-478.5	133.4359	150.3113	158.3631	162.9176
-332.5	158.7407	163.5391	166.0832	167.1073
-169.25	167.8916	169.4473	169.9645	170.9831
0.25	171.9969	171.9981	171.9984	171.9993
169.75	168.1452	169.1133	170.0830	171.0536
332.75	158.3841	163.4021	166.3457	167.3409
478.5	133.8930	150.1664	158.0518	162.3984

In Table 3-2, the central location of each experimental cosine peak is the same as the data in the fourth column of Table 3-1. The remaining contents indicate data from different surfaces using the first column data as the abscissa to fit the values via the cubic interpolation method. Now, these four columns of data have been compared with the experimentally obtained cosine period number data, as shown in the first column of Table 3-3. Each point's error has been obtained by subtracting the simulated value from the experimentally obtained value in sequence. All the errors have been calculated and demonstrated. The last row in the table above represents the root mean square error (RMSE), which refers to the square root of the sum of the squares of the differences divided by the number of points. It can be concluded from the four RMSEs that the data in the case of $e = 1$ is the closest to the experiment.

Table 3-3: The error analysis of experimental and fitted period number data in four cases

Experimental Period (in pixels)	$e = 1.0$ Data Error (pixels)	$e = 1.1$ Data Error (pixels)	$e = 1.2$ Data Error (pixels)	$e = 1.3$ Data Error (pixels)
133	0.4359	17.3113	25.3631	29.9176
159	-0.2593	4.5391	7.0832	8.1073
167.5	0.3916	1.9473	2.4645	3.4831
171.5	0.4969	0.4981	0.4984	0.4993
167.5	0.6452	1.6133	2.5830	3.5536
158.5	-0.1159	4.9021	7.8457	8.8409
133	0.8930	17.1664	25.0518	29.3984
RMSE	0.5189	9.6039	14.1199	16.5970

For further demonstration of the proximity of two sets of data, the slopes between adjacent points have also been calculated. In Table 3-4, the first column represents the six slope values obtained from seven experimental data points. Next, the slopes between adjacent fitted points have been acquired for each simulated surface. Finally, the four RMSEs have been calculated as described earlier. As can be seen from the results, the surface of $e = 1$ is, once again, the closest to the experimental data.

The comparisons above conclusively prove that the case $e = 1.0$ is most consistent with the experimental results. Accordingly, the reconstructed surface morphology of the transparent object is as shown in Figure 3-16 (a), which is in excellent agreement to the actual shape of the transparent object which is photographed and measured, as shown in Figure 3-16 (b). All coordinate units in Figure 3-16 (a) have been converted to centimeters to represent the actual length. Besides, while only the curved surface has been shown, the blank space in the middle should be filled with clear glass. The vertical red line in Figure 3-16 (b) has been measured as $10\ cm$. In

the reconstructed surface results, the highest point is exactly $10\ cm$ from the zero plane, which agrees with the conclusion $e = 1$, implying that the object is a semi-circular block of glass.

Table 3-4: Slope analysis of experimental and fitted period data for four ellipticities.

Experimental Slope	Slope for $e = 1.0$	Slope for $e = 1.1$	Slope for $e = 1.2$	Slope for $e = 1.3$
0.1781	0.1733	0.0906	0.0529	0.0287
0.0521	0.0561	0.0362	0.0238	0.0237
0.0236	0.0242	0.0150	0.0120	0.0060
-0.0236	-0.0227	-0.0170	-0.0113	-0.0056
-0.0552	-0.0599	-0.0350	-0.0229	-0.0228
-0.1750	-0.1680	-0.0908	-0.0569	-0.0339
RMSE	0.0043	0.0508	0.0727	0.0863

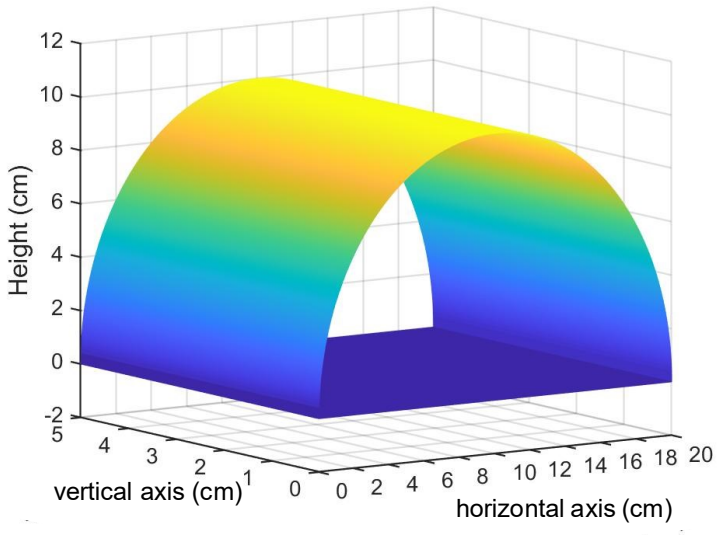

(a)

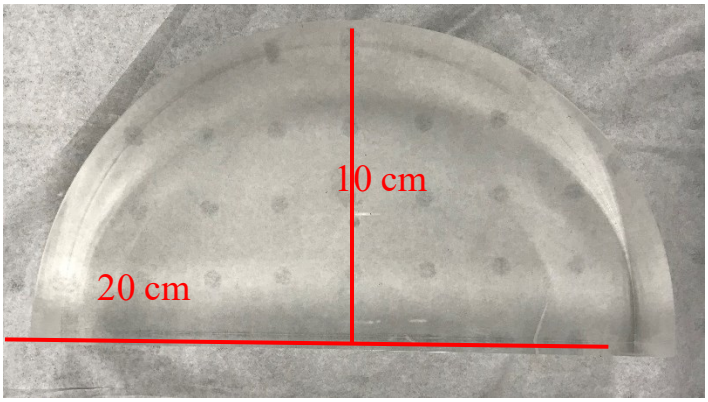

(b)

Figure 3-16: The morphology of the target transparent object. (a) The simulated surface result; (b) the actual shape of the transparent object.

3.3.3 Transparent Parabolic Cylinder Reconstruction

Based on the successful reconstruction of the first transparent object, another cylinder with an unknown cross-section shape (see Figure 3-17 (a)) has been used in the second experiment. Following the procedure in Section 3.3.2, the reference fringe and deformed pattern have been extracted from the captured image, and is shown in Figures 3-17 (b,c).

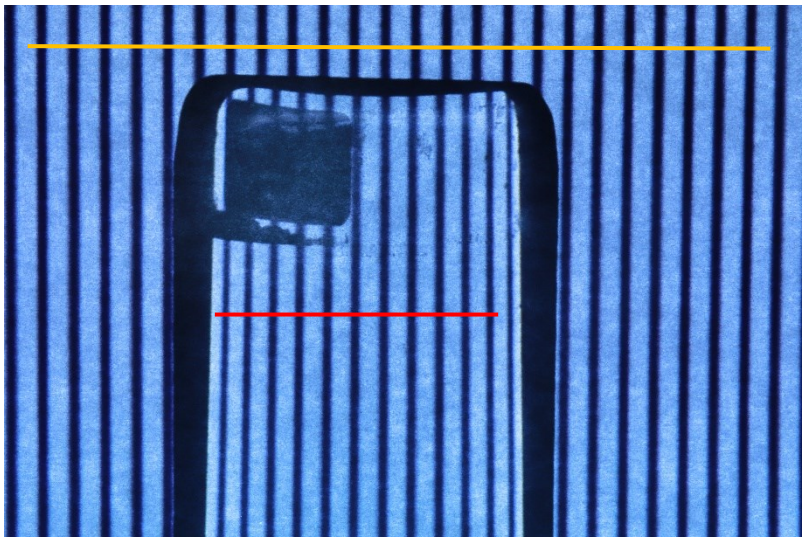

(a)

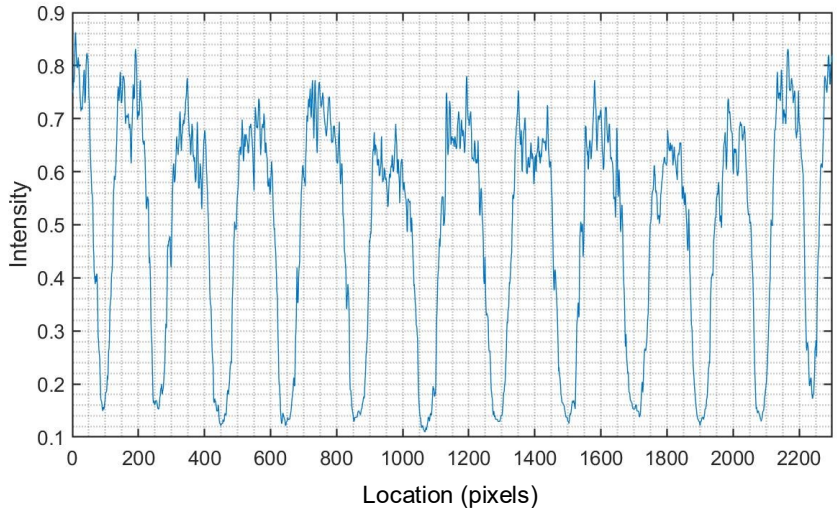

(b)

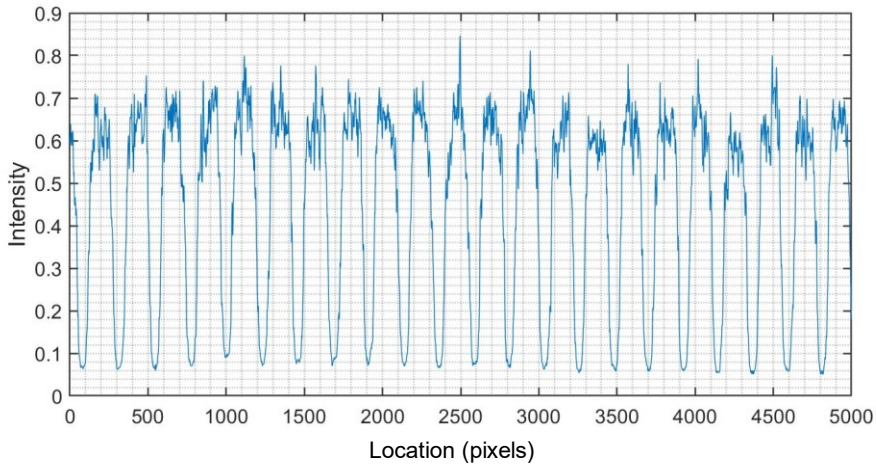

(c)

Figure 3-17: The illustration of the reference and deformed pattern. (a) The captured image including both reference and deformed image area; (b) The intensity distribution of one extracted horizontal line from the deformed pattern, shown in red in (a); (c) The intensity distribution of one extracted horizontal line from the reference pattern, shown in yellow in (a). One pixel represents about 20 microns.

As before, each valley point has been found; and thereafter, the periods (in pixels) and their center positions (also in pixels) are calculated and shown in Table 3-5. The results are plotted in Figure 3-18 where successive experimental points are joined using splines. Also superposed are representative numerically generated plots with different ellipticities.

Table 3-5: Data processing for the second transparent object

Valley Location (Pixel #)	Period (in pixels)	Central Location (Pixel #)	Translated Central Location (Pixel #)
95			
259	164	177	-994.75
444	185	351.5	-820.25
644	200	544	-627.75
852.5	208.5	748.25	-423.5
1066	213.5	959.25	-212.5
1281.5	215.5	1173.75	2
1495.5	214	1388.5	216.75
1703	207.5	1599.25	427.5
1902	199	1802.5	630.75
2086	184	1994	822.25
2250	164	2168	996.25

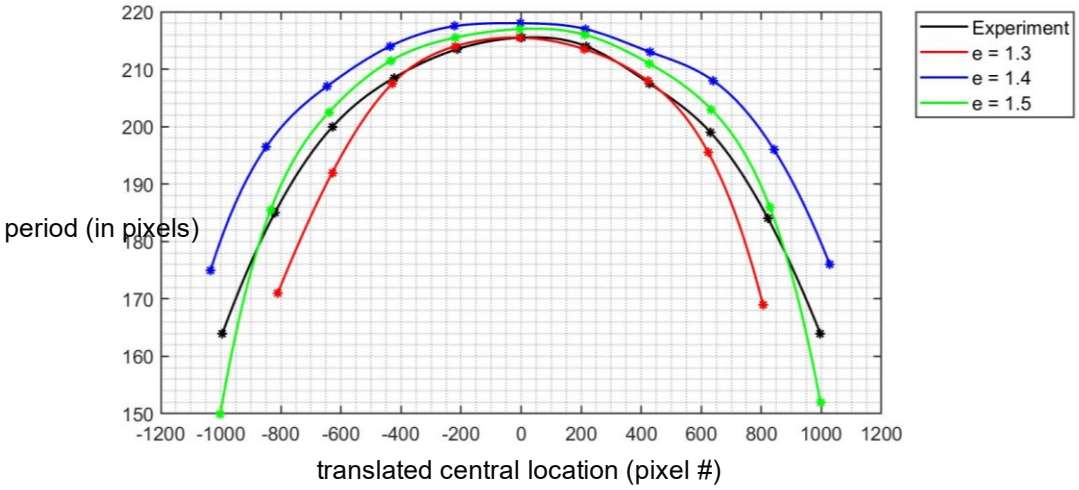

Figure 3-18: Cosine periods in pixels vs. peak central location data for the experiment and three simulated surfaces with different ellipticities. Different colors indicate different ellipticities of objects, as shown in the top-right label. One pixel represents about 20 microns.

From the simulation results of three typical semi-elliptical cylinders shown above, it can be concluded none of them are candidates for a good fit. The red curve ($e = 1.3$) agrees well with the experimental data (black line) in the middle, but the slope changes too much away from the center. The blue curve ($e = 1.4$) has a trend similar to the experimental curve but the values of the period are consistently higher. Finally, the green curve ($e = 1.5$) seems closest to the experimental curve overall, but its RMSE is expected to be large. All of these attempts point to the fact that an elliptical fitting is not the best choice for this case.

Parabolic shapes are now tried. The parabola is taken as $y = ax^2$, where a is a parameter that can be varied, similar to the ellipticity e in the previous case. This can also give rise to varying periods similar to what is experimentally observed. Results using three representative values of a are plotted along with the experimental results in Figure 3-19. This time, the fit appears much closer; therefore, values of a equal to $a = -2.15 \times 10^{-4}$ and $a = -2.16 \times 10^{-4}$ have been attempted.

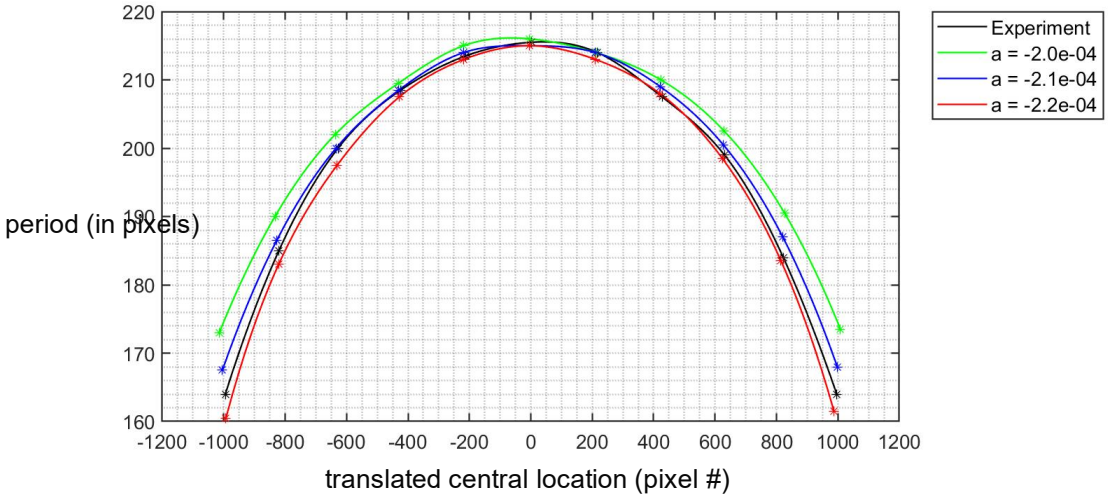

Figure 3-19: Cosine periods in pixels vs. peak central location data for the experiment and three simulated parabolic cylinders with different curvatures. Different colors indicate different parameters of simulated surfaces, as shown in the top-right label. One pixel represents about 20 microns.

Noting that the value of a should be between $a = -2.1 \times 10^{-4}$ and $a = -2.2 \times 10^{-4}$, various values of a were attempted in steps of $a = -0.01 \times 10^{-4}$. Typical error analysis results using $a = -2.15 \times 10^{-4}$ and $a = -2.16 \times 10^{-4}$ are shown in Tables 3-6 (a,b). The results show the best fitting for $a = -2.16 \times 10^{-4}$. The RMSE error of less than $0.5\ pixels$ is lower than the minimum resolution of $1\ pixel$. Using this value of a, the maximum height H of the curved surface is obtained as $444.1729\ pixels$, which corresponds to a computed height of $8.982576\ mm$, for a pixel size of $49.45\mu m$. The pixel size has been determined using a procedure similar to that in the previous example. The true measured height is $9\ mm$, and corresponds to an error of 0.1936%. The error can theoretically be further minimized by using even finer resolution in the value of a.

Table 3-6: Error analysis for parabolic cylinder object. (a) Period data of experiment and fitting via cubic interpolation method according to the experimental peak central location. (b) Slope analysis of the experimental and fitted data in (a).

Experimental Period (in pixels)	$a = -2.15 \times 10^{-4}$ Fitted Period (in pixels)	$a = -2.16 \times 10^{-4}$ Fitted Period (in pixels)
164	165.0315	163.4025
185	184.8645	184.8287
200	199.2741	199.2369
208.5	208.6531	208.1543
213.5	213.0718	213.0740
215.5	214.9990	214.9990
214	213.9434	213.9435
207.5	207.7961	207.7906
199	199.2043	198.6795
184	185.0868	184.5209
164	164.0001	163.8752
RMSE	0.5544	0.4262

(a)

Experimental Slope	Slope for $a = -2.15 \times 10^{-4}$	Slope for $a = -2.16 \times 10^{-4}$
0.1203	0.1137	0.1228
0.0779	0.0749	0.0748
0.0416	0.0459	0.0437
0.0237	0.0209	0.0233
0.0093	0.0090	0.0090
-0.0070	-0.0049	-0.0049
-0.0308	-0.0292	-0.0292
-0.0418	-0.0423	-0.0448
-0.0783	-0.0737	-0.0739
-0.1149	-0.1212	-0.1187
RMSE	0.0038	0.0026

(b)

The 3D perspective of the reconstruction result of the target morphology is shown in Figure 3-20.

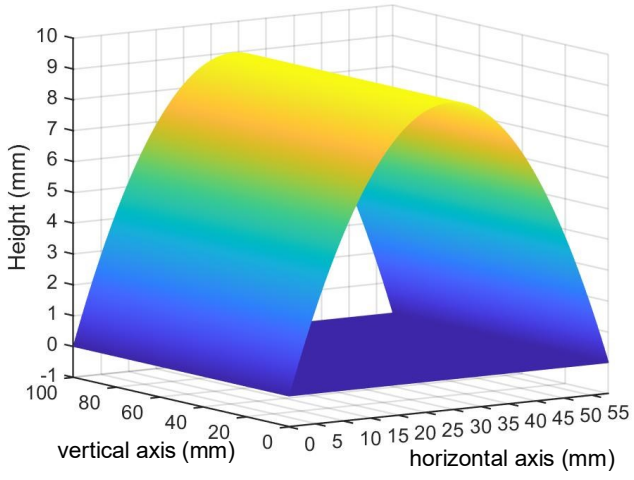

(a)

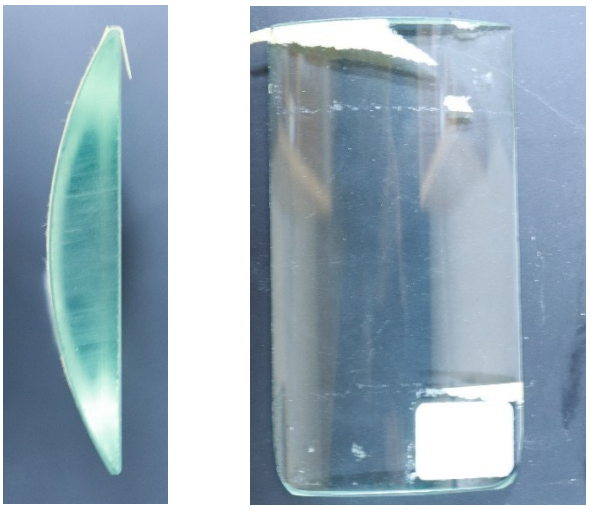

(b) (c)

Figure 3-20: The morphology of the target transparent object: (a) resulting simulated surface; (b, c) two views of the transparent object.

3.3.4 Transparent Bi-cylinder Reconstruction

To further verify the feasibility and universality of our proposed method, a third glass object with two curved surfaces has been used as a third test case, as shown in Figure 3-21. Its long side, as shown as the yellow line below, is slightly less than $10\ cm$. The detailed lengths of these three colored lines will be described later to compare with reconstructed results. Similar to the previous examples, the undeformed and deformed fringe pictures are shown in Figure 3-22.

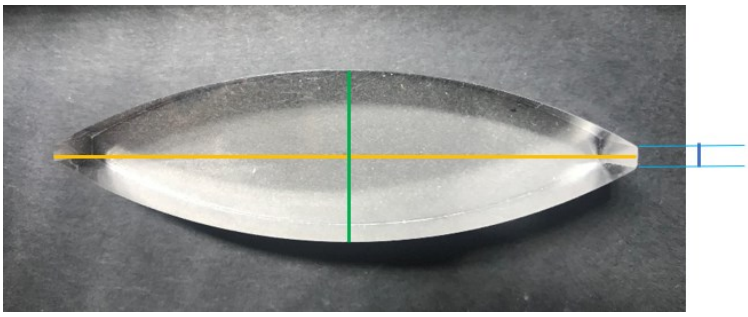

Figure 3-21: Top view of test object.

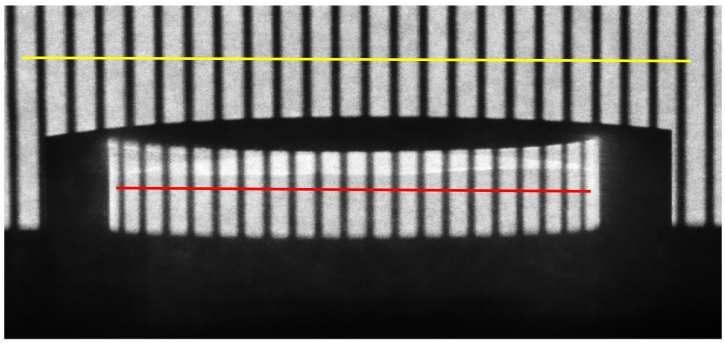

(a)

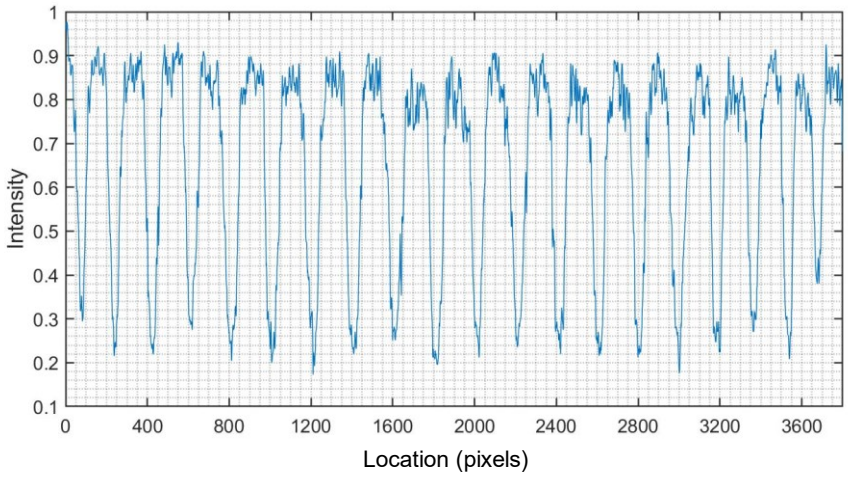

(b)

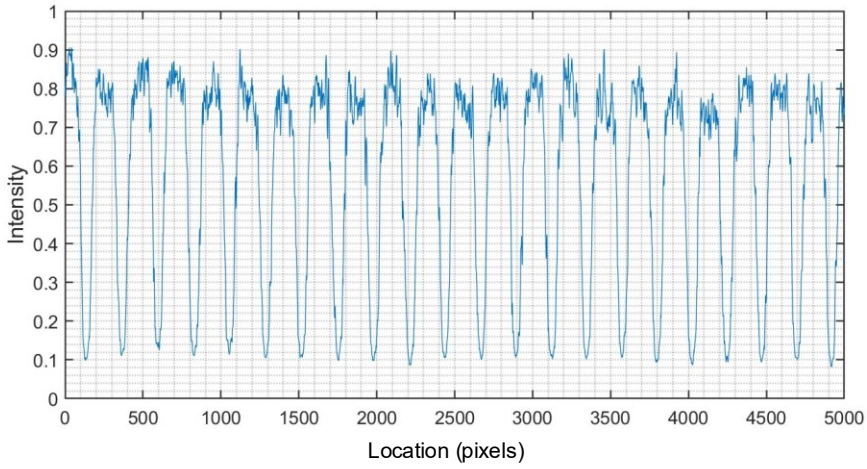

(c)

Figure 3-22: Illustration of the reference and deformed patterns. (a) Captured image including both reference and deformed image area; (b) intensity distribution of one extracted horizontal line from the deformed pattern, shown in red in (a); (c) intensity distribution of one extracted horizontal line from the reference pattern, shown in yellow in (a).

After processing Figure 3-22(b), the records of experimental data are shown Table 3-7.

Table 3-7: Data processing for the third experimental transparent object.

Valley Location (Pixel #)	Period (in pixels)	Central Location (Pixel #)	Translated Central Location (Pixel #)
161			
313	152	237	-1727.63
488.5	175.5	400.75	-1563.88
675.5	187	582	-1382.63
870	194.5	772.75	-1191.88
1066	196	968	-996.625
1267.5	201.5	1166.75	-797.875
1468.5	201	1368	-596.625
1672.5	204	1570.5	-394.125
1872	199.5	1772.25	-192.375
2075	203	1973.5	8.875
2275	200	2175	210.375
2478.5	203.5	2376.75	412.125
2678	199.5	2578.25	613.625
2878	200	2778	813.375
3074.5	196.5	2976.25	1011.625
3267	192.5	3170.75	1206.125
3451	184	3359	1394.375
3620.5	169.5	3535.75	1571.125
3764	143.5	3692.25	1727.625

Unlike the distributions of the period for the previous examples, this data when plotted no longer looks like a simple parabola, but rather has some fluctuations, as shown in Figure 3-23. This difference may stem from the fact that light rays converging at the first contact surface may be diverged at the second surface, or even reflected back into the object to create dark areas on either side.

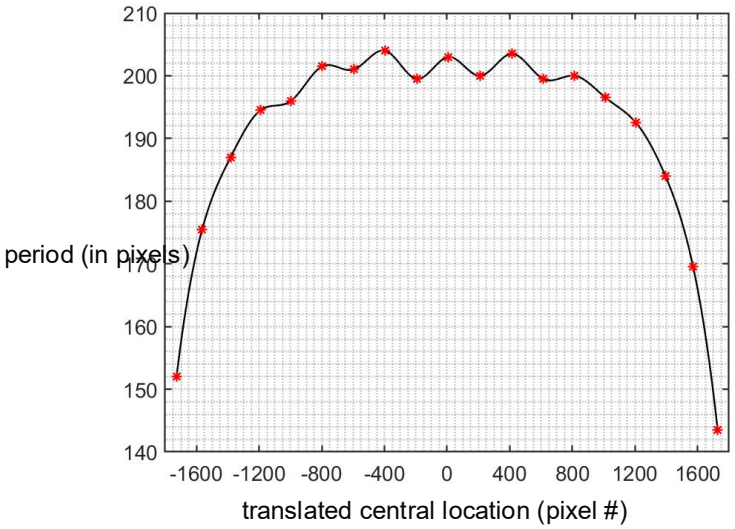

Figure 3-23: Variation of period with translated central location. One pixel represents approximately 16 microns.

As before, the red asterisks in the figure above are data from Table 3-7, while the black curve is just for a smooth connection to observe its overall trend. From Figure 3-22, the period of the projected cosine pattern on the imaging plane is 226.8 pixels. The maximum distance between the black area on two sides in Figure 3-22 (a) is 4930 pixels, which can be used as the illumination zone incident to the object. Its corresponding length is accurately measured as $78.5\ mm$. Thus, the spatial resolution is obtained as $15.923\ \mu m/pixel$.

Since this transparent product is composed of cylindrically shaped surfaces, a numerically generated cosine pattern of period 226.8 pixels and also occupying 4930 pixels is used for simulation. Many parabolic surfaces have been tried in the simulations to match the experimental cosine period data (for processing code, see Appendix). For the record, the object has not been

initially pre-judged as two identical parabolas of opposite curvatures, so asymmetrical shapes of the upper and lower surfaces have also been extensively explored. However, in the process of continuous optimization, it is found that the test object is indeed symmetrical. The final cross-sectional picture using parabolas with $a = -0.000109301$ for the top surface and $a = 0.000109301$ for the bottom surface is shown in Figure 3-24. Also shown is the experimental results along with the fitted results for the period.

Error analysis (not shown here for brevity) shows that the RMSE of the slopes is of the order of 10^{-4}, which indicates good agreement between simulation and experimental data. To verify the reconstruction, the green and blue lines in Figure 3-21 are measured as $23.5\,mm$ and $2.35\,mm$ respectively by a micrometer. Now, the numbers of pixels occupied by them are 1487.3 and 150, which can be converted to $23.6822\,mm$ and $2.3884\,mm$ using the spatial resolution derived above. Their errors are calculated as 0.7753% and 1.6340% respectively, which is assumed to be acceptable.

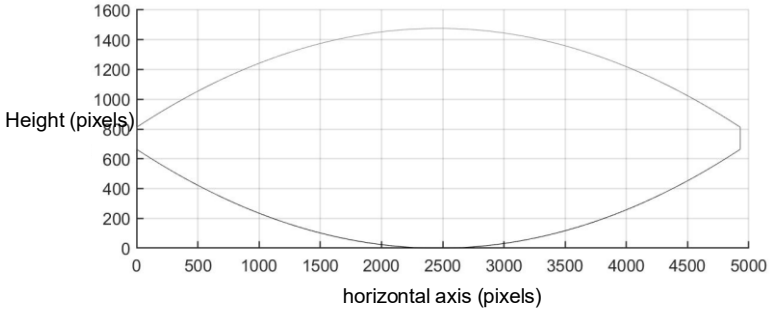

(a)

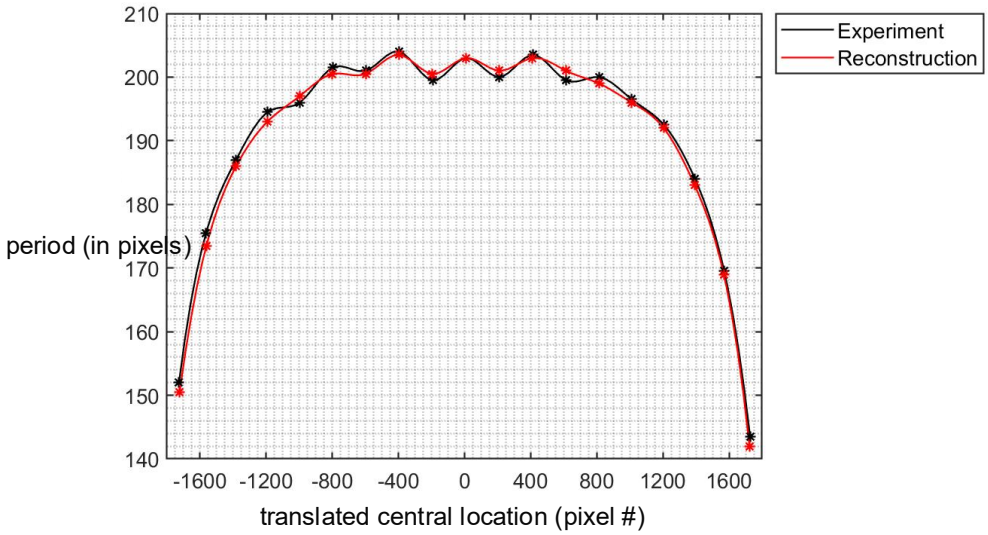

(b)

Figure 3-24: (a) Cross-section of the simulation results with $a = -0.000109301$ for the top surface and $a = -0.000109301$ for the bottom surface; (b) comparison of experimental and simulated results for the period. One pixel represents approximately $16\ \mu m$.

The 3D reconstructions in units of actual lengths is shown in Figure 3-25.

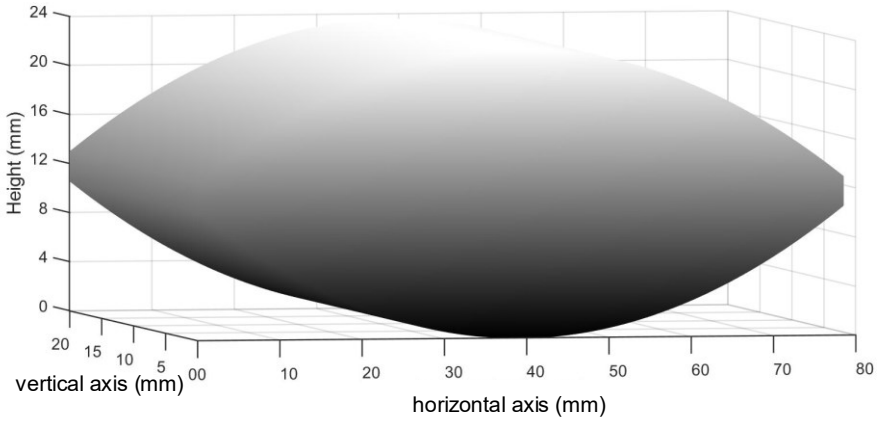

Figure 3-25: The final 3D reconstruction results in units of actual lengths.

3.4 Discussion and Conclusion

3.4.1 Effect of Imaging Distance

In our error analysis process, in addition to the positional error of each discrete point (type I error), the error in the slope between adjacent points (type II error) is also taken into account. In

the cases shown above, the simulated morphology with the smallest type I error also has the smallest RMSE of slope values. However, it is possible these two errors may not be minimized at the same time. Investigation of the imaging distance is the key to exploring this issue.

As shown in Figure 3-1 in Section 3.2.2, the imaging plane right against the apex of the phase object, implying that the separation distance d is equal to zero. However, d cannot be exactly equal to zero in reality. This practical issue can be ignored for large objects, but should be considered for millimeter-scale targets.

As an illustration, the spatial variation of the period resulting from a semi-elliptical cylinder with an ellipticity of $e = 1.3$, made of glass with refractive index of 1.5, but for different values of d has been simulated and plotted below. The reference cosine pattern has a width of $4000\ pixels$ and a period of $100\ pixels$.

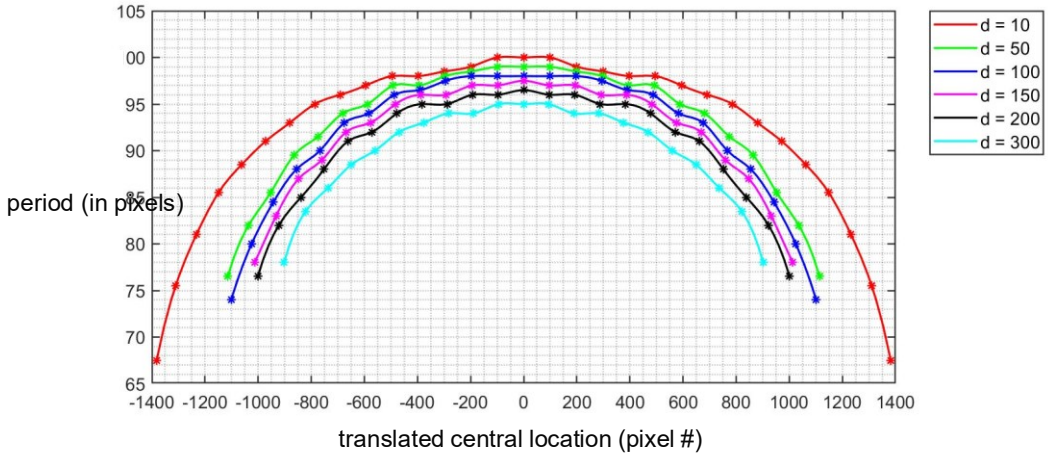

Figure 3-26: The plotted cosine period vs. translated peak center position data for six cases with varied imaging distances. Different colors indicate different values of d (in pixels), as shown in the top-right label.

The maximum height of simulated surface is 722 pixels, which is much larger than the above values of d. The curves seem to shrink proportionally as d increases, presumably due to the convergence of light rays. Furthermore, the consistency of the slope distributions of these curves can be verified by some simple calculations.

In general, it is observed that a decreasing slope error is a good indicator for the optimization direction in the reconstruction process. If the type I error is large, but the type II error is small, it is likely that the simulated morphology is close to the correct answer, but the setting of d is not correct. Therefore, d should be modified at this time before optimizing the surface shape. This finding is especially useful in some cases where the imaging plane cannot be physically right against the surface. It is worth noting that the numerical change of d has no obvious effect on the result within $10\ pixels$.

3.4.2 Discussion of Complex Surfaces

In general, reconstruction of complex surfaces of transparent objects is a complicated process. Almost all target objects used in the common methods such as polarization imaging, reflection reconstruction method, distortion recovery method, and spectral confocal method are composed of simple, unfolded, and non-self-occlusion surfaces. Even many of them have only one curved surface.

In this Chapter, two transparent cylinders with only one undetermined surface have been reconstructed via our proposed method and verified by extremely small RMSEs. Furthermore, a third example has also demonstrated good results for a multi-faceted case. Crucially, the basis of our light propagation model is the one-to-one relationship between the object morphology and the spatial variation of the period of the deformed pattern image. As long as this condition is satisfied, straightforward simulations can derive the actual shape using the required information from a picture of the deformed pattern.

The experiments that have been done so far are just a variety of cylinders, meaning that the cross-section at every height is exactly the same. Even so, more complicated transparent objects can be completely reconstructed based on this technique. For instance, each row of the deformed image can be performed the identical operation as before, one by one. Then, the shape of each

cross-section can be determined. After integration, the whole 3D morphology can be obtained. This idea can be implemented in highly complex objects with varying and steep surfaces. Since, in our examples, only one row of pixel information needs to be analyzed simultaneously, the complexity can be greatly reduced.

For objects slightly more complex than cylinders, but without many other variations, our analysis can be readily extended. For example, starting with an approximately ellipsoidal surface, its deformed image can be simulated and analyzed. Next, some parameters of the surface should continuously be optimized until a satisfactory error result appears. In this process, how to determine the direction of parameter optimization is a key point. In our reported work, the ellipticity or parabolic curvature has been used as an optimization parameter to get closer to the real surface. When the error with the experimental data is small enough, the simulated object can be considered the final result.

Theoretically, no matter whether a logical direction of surface optimization is applied, the reconstruction can be completed only if enough deformed images can be simulated and their errors can be calculated. However, small features require relatively dense cosine fringes as the reference image to record details. Correspondingly, a high-quality camera is also necessary. Both can bring richer information and higher resolution, which equates to more data processing power. Therefore, it is a time-saving and computation-saving solution to establish a mechanism for efficiently performing parameter optimization.

Deep learning is another powerful tool that can be of advantage. If a large number of objects can be tested in advance and their data can be retained in the library, then it will be quick and convenient to call the original database for correction and optimization when the new objects are reconstructed. The larger the database, the more accurate the model will be, but also more time will be taken to train.

The above discussion is to demonstrate the practicality and universality of our proposed method. Although very complex objects have not been used for reconstruction in the current work, the solutions presented in this Section are quite reasonable and effective. In general, the reconstruction of complex transparent objects is exceedingly difficult, but the concept presented here makes it greatly promising.

CHAPTER IV

CONCLUSIONS AND FUTURE WORK

4.1 Conclusions

In this thesis, the reconstructions of amplitude objects with 3D topography and 3D transmissive phase objects of various sizes and shapes are presented, using structured light as a probing optical tool.

In Chapter I, different 3D reconstruction methods, both holographic and nonholographic, are reviewed. In addition, the similarities between using structured light and ghost imaging and OSH are discussed.

In Chapter II, a single-shot digital phase-shifting Moiré pattern method for 3D topography of an amplitude object based on FPP using structured light is proposed. In this technique, the phase information of the object is obtained by superposing the digitally generated reference cosine fringes and the captured deformed image. Multiple shots are not required since the Moiré patterns are generated by digitally phase shifting the reference fringes. Besides, using laser interference fringes instead of the traditional projection of a periodic intensity pattern can readily give adjustable fringe periods and thus improve the resolution of the experiments, although the principle of structured light illumination is inherently incoherent. The effects of speckle noise, however, remains to be determined.

In Chapter III, a simple concept of light refraction due to change of refractive index and curvature of the interface provides a straightforward way to reconstruct transparent phase objects with projected structured light. The ray propagation model allows the target shape to be deduced from just one captured deformed image. The simplicity and directness of this approach is an obvious advantage. If our proposed method can be combined with deep learning, then complex morphology reconstruction is possible.

The work reported in Chapter II has been presented at *OSA 2020 Digital Holography and Three-Dimensional Imaging Meeting* [103] and published in Applied Optics [104]. The work reported in Chapter III will be presented at the upcoming *OSA 2021 Digital Holography and Three-Dimensional Imaging Meeting* [105].

4.2 Future Work

Structured light is an extremely powerful technology with a huge market for commercial applications. Therefore, exploring the advantages of our proposed methods and continuously optimizing the accuracy, resolution and robustness should be the direction of future efforts. The shortcomings of AM reconstruction in Chapter II point out the necessity of capturing higher-quality pictures and eliminating noise (viz., speckle) via better digital image processing techniques. Moreover, more sophisticated signal and image processing techniques can further reduce the processing time, necessitating the need to design the optimum digital filter.

Introduction of deep learning to structured light probing is another area of future research. Optimizing the surface shape of transparent objects as shown in Chapter III still needs considerable time, but the establishment of a suitable training database and use of forward and inverse neural networks can help in accurately predicting the profile of the phase object. Also, using neural networks to find optimal digital filters for Moiré pattern analysis could be beneficial for determining the accurate 3D surface topography of amplitude objects.

REFERENCES

4. F. Remondino and S. El-Hakim, “Image-based 3D modelling: a review,” Photogramm. Rec. **21**, 269-291(2006).

5. J. J. Aguilar, F. Torres, and M. A. Lope, “Stereo vision for 3D measurement: accuracy analysis, calibration and industrial applications,” Measurement **18**, 193-160 (1996).

6. S. Slob and R. Hack, “3D terrestrial laser scanning as a new field measurement and monitoring technique,” in R. Hack, R. Azzam, and R. Charlier (ed.) *Engineering geology for infrastructure planning in Europe. Lecture Notes in Earth Sciences*, **104**, Springer (2004).

7. S. F. El-Hakim, J. A. Beraldin, M. Picard, and G. Godin, “Detailed 3D reconstruction of large-scale heritage sites with integrated techniques,” IEEE Comput. Graph. Appl. **24**, 21-29 (2004).

8. Y. Park, C. Depeursinge, and G. Popescu, “Quantitative phase imaging in biomedicine,” Nat. Photon. **12**, 578-589 (2018).

9. D. Jiang, Y. Hu, S. Yan, L. Zhang, H. Zhang, and W. Gao, “Efficient 3D reconstruction for face recognition,” Pattern Recognition **38**, 787-798 (2005).

10. K. C. Wong, S. M. Kumta, K. H. Chiu, G. E. Antonio, P. Unwin, and K. S. Leung, “Precision tumour resection and reconstruction using image-guided computer navigation,” J. Bone Joint Surg. Br. **89**, 943-947 (2007).

11. J. Gao, X. Chen, O. Yilmaz, and N. Gindy, "An integrated adaptive repair solution for complex aerospace components through geometry reconstruction," Int'l. J. Adv. Manuf. Technol. **36**, 1170-1179 (2008).

12. M. Vázquez-Arellano, H. W. Griepentrog, D. Reiser, and D. S. Paraforos, "3-D imaging systems for agricultural applications—a review," Sensors **16**, 618 (2016).

13. A. Verhulst, M. Hol, R. Vreeken, A. Becking, D. Ulrich, and T. Maal, "Three-dimensional imaging of the face: a comparison between three different imaging modalities," Aesthet. Surg. J. **38**, 579-585 (2018).

14. G. Bradshaw, *Non-contact Surface Geometry Measurement Techniques*, MS Thesis, Trinity College Dublin, Department of Computer Science (1999).

15. A. Wehr and U. Lohr, "Airborne laser scanning—an introduction and overview," ISPRS J. Photogramm. Remote Sensing **54**, 68-82 (1999).

16. T. C. Poon, K. B. Doh, B. W. Schilling, M. H. Wu, K. K. Shinoda, and Y. Suzuki, "Three-dimensional microscopy by optical scanning holography," Opt. Eng. **34**, 1338-1345 (1995).

17. T. Takamatsu and S. Fujita, "Microscopic tomography by laser scanning microscopy and its three-dimensional reconstruction," J. Microscopy **149**, 167-174 (1988).

18. G. Nehmetallah and P. P. Banerjee, "Applications of digital and analog holography in three-dimensional imaging," Adv. Opt. Photonics **4**, 472-553 (2012).

19. B. Cyganek and J. P. Siebert, *An Introduction to 3D Computer Vision Techniques and Algorithms*. John Wiley & Sons (2011).

20. X. Wang, Y. Cao, W. Cui, X. Liu, S. Fan, Y. Zhou, and Y. Li, "Three-dimensional range-gated flash LIDAR for land surface remote sensing," Proc. SPIE **9260**, 92604L (2014).

21. F. Chen, G. M. Brown, and M. Song, "Overview of 3-D shape measurement using optical methods," Opt. Eng. **39**, 10-22 (2000).

22. J. W. Goodman, *Introduction to Fourier Optics.* Roberts and Company Publishers (2005).

23. E. Cuche, F. Bevilacqua, and C. Depeursinge, "Digital holography for quantitative phase-contrast imaging," Opt. Lett. **24**, 291-293 (1999).

24. B. Cyganek, and J. P. Siebert, *An Introduction to 3D Computer Vision Techniques and Algorithms.* John Wiley & Sons (2011).

25. R. Szeliski, *Computer Vision: Algorithms and Applications*. Springer Science & Business Media (2010).

26. O. Faugeras, and O. A. FAUGERAS, *Three-dimensional Computer Vision: A Geometric Viewpoint.* MIT press (1993).

27. J. Geng, "Structured-light 3D surface imaging: a tutorial," Adv. Opt. Photonics **3**, 128-160 (2011).

28. D. L. Andrews, *Structured Light and its Applications: An Introduction to Phase-structured Beams and Nanoscale Optical Forces*. Academic (2011).

29. R. J. Valkenburg and A. M. McIvor, "Accurate 3D measurement using a structured light system," Image Vis. Comp. **16**, 99-110 (1998).

30. S. Wang, P. C. Wu, V. C. Su, Y. C. Lai, M. K. Chen, H. Y. Kuo, B.H. Chen, Y.H. Chen, T.T. Huang, J. H. Wang, and R. M. Lin, "A broadband achromatic metalens in the visible," Nature Nanotechnology **13**, 227-232 (2018).

31. G. Steiner, "Surface plasmon resonance imaging," Anal. Bioanal. Chem. **379**, 328-331(2004).

32. L. Waller, L. Tian, and C. Barbastathis, "Transport of intensity phase-amplitude imaging with higher order intensity derivatives," Opt. Exp. **18**, 12552-12561 (2010).

33. Y. Rivenson, Y. Wu, and A. Ozcan, "Deep learning in holography and coherent imaging," Light Sci. Appl. **8**, 1-8 (2019).

34. A. Sinha, J. Lee, S. Li, and G. Barbastathis, "Lensless computational imaging through deep learning," Optica **4**, 1117-1125 (2017).

35. K. Khare, *Fourier Optics and Computational Imaging.* John Wiley & Sons (2015).

36. M. Levoy, "Light fields and computational imaging," Computer **39**, 46-55 (2006).

37. T. E. Gureyev, D. M. Paganin, A. Kozlov, Y. I. Nesterets, and H. M. Quiney, "Complementary aspects of spatial resolution and signal-to-noise ratio in computational imaging," Phys. Rev. A **97**, 053819 (2018).

38. J. Batlle, E. Mouaddib, and J. Salvi, "Recent progress in coded structured light as a technique to solve the correspondence problem: a survey," Pattern Recognition **31**, 963-982 (1998).

39. J. Salvi, J. Pages, and J. Batlle, "Pattern codification strategies in structured light systems," Pattern Recognition **37**, 827-849 (2004).

40. C. Quan, W. Chen, and C. J. Tay, “Phase-retrieval techniques in fringe-projection profilometry,” Opt. Lasers Eng. **48**, 235-243 (2010).

41. Z. Wang, D. A. Nguyen, and J. C. Barnes, “Some practical considerations in fringe projection profilometry,” Opt. Lasers Eng. **48**, 218-225 (2010).

42. R. Porras-Aguilar and K. Falaggis, “Absolute phase recovery in structured light illumination systems: Sinusoidal vs. intensity discrete patterns,” Opt. Lasers Eng. **84**, 111-119, (2016).

43. H. Du and Z. Wang, “Three-dimensional shape measurement with an arbitrarily arranged fringe projection profilometry system,” Opt. Lett. **32**, 2438-2440 (2007).

44. Z. Guo, J. Wang, Y. Zhu, S. Rong, Y. Song, and P. P. Banerjee, “Dynamic phase retrieval for fringe image processing in Moiré tomography,” Proc. SPIE **11249**, 1124921 (2020).

45. H. Takasaki, “Moiré topography,” Appl. Opt. **9**, 1467-1472 (1970).

46. Y. Bromberg, O. Katz, and Y. Silberberg, “Ghost imaging with a single detector," Phys. Rev. A **79**, 053840 (2009).

47. J. H. Shapiro, “Computational ghost imaging,” Phys. Rev. A **78**, 061802 (2008).

48. B. I. Erkmen, and J. H. Shapiro, “Unified theory of ghost imaging with Gaussian-state light,” Phys. Rev. A **77**, 043809 (2008).

49. J. H. Shapiro, and R. W. Boyd, “The physics of ghost imaging,” Quantum Inf. Process. **11**, 949-993 (2012).

50. Z. Zhang, X. Ma, and J. Zhong, “Single-pixel imaging by means of Fourier spectrum acquisition,” Nature Commun. **6**, 1-6 (2015).

51. L. Martínez-León, P. Clemente, Y. Mori, V. Climent, J. Lancis, and E. Tajahuerce, "Single-pixel digital holography with phase-encoded illumination," Opt. Exp. **25**, 4975-4984 (2017).

52. D. J. Zhang, Q. Tang, T. F. Wu, H. C. Qiu, D. Q. Xu, H. G. Li, H. B. Wang, J. Xiong, and K. Wang, "Lensless ghost imaging of a phase object with pseudo-thermal light," Appl. Phys. Lett. **104**, 121113 (2014).

53. T. C. Poon, *Optical Scanning Holography with MATLAB*. Springer (2007).

54. T. C. Poon, K. B. Doh, B. W. Schilling, M. H. Wu, K. K. Shinoda, and Y. Suzuki, "Three-dimensional microscopy by optical scanning holography," Opt. Eng. **34,** 1338-1344 (1995).

55. T. C. Poon, T. Kim, G. Indebetouw, B. W. Schilling, M. H. Wu, K. Shinoda, and Y. Suzuki, "Twin-image elimination experiments for three-dimensional images in optical scanning holography," Opt. Lett. **25,** 215-217 (2000).

56. T. C. Poon, "Optical scanning holography-a review of recent progress," J. Opt. Soc. Korea **13**, 406-415 (2009).

57. M. A. A. Neil, A. Squire, R. JusĬkaitis, P. I. H. Bastiaens, and T. Wilson, "Wide-field optically sectioning fluorescence microscopy with laser illumination," J. Microscopy **197**, 1-4 (2000).

58. H. Lin, J. Gao, Q. Mei, G. Zhang, Y. He, and X. Chen, "Three-dimensional shape measurement technique for shiny surfaces by adaptive pixel-wise projection intensity adjustment," Opt. Lasers Eng. **91**, 206-215 (2017).

59. C. A. Walker, "A historical review of Moiré interferometry," Exp. Mech. **34**, 281-299 (1994).

60. H. Ding, R. E. Powell, C. R. Hanna, and I. C. Ume, "Warpage measurement comparison using shadow Moiré and projection Moiré methods," IEEE Trans. Comp. Packaging Mfg. Tech. **25**, 714-721 (2002).

61. L. Pirodda, "Shadow and projection Moiré techniques for absolute or relative mapping of surface shapes," Opt. Eng. **21**, 214640 (1982).

62. R. Torroba and A. A. Tagliaferri, "Precision small angle measurements with a digital Moiré technique," Opt. Commun. **149**, 213-176 (1998).

63. K. J. Gasvik, "Moire technique by means of digital image processing," Appl. Opt. **22**, 3543-3548 (1983).

64. S. De Nicola and P. Ferraro, "Fourier transform method of fringe analysis for Moiré interferometry," J. Opt. A: Pure Appl. Opt. **2**, 228-233 (2000).

65. C. Zuo, S. Feng, L. Huang, T. Tao, W. Yin, and Q. Chen, "Phase shifting algorithms for fringe projection profilometry: A review," Opt. Lasers Eng. **109**, 23-59 (2018).

66. V. Srinivasan, H. C. Liu, and M. Halioua, "Automated phase-measuring profilometry of 3-D diffuse objects," Appl. Opt. **23**, 3105-3108 (1984).

67. J. A. Buytaert and J. J. Dirckx, "Design considerations in projection phase-shift Moiré topography based on theoretical analysis of fringe formation," J. Opt. Soc. Amer. A **24**, 2003-1613 (2007).

68. Y. B. Choi, and S. W. Kim, "Phase-shifting grating projection Moiré topography," Opt. Eng. **37**, 1005-1010 (1998).

69. Y. Zhu, H. Wen, H. Zhang, and Z. Liu, “Application of digital phase shifting moiré method in interface and dislocation location recognition and real strain characterization from HRTEM images,” Opt. Exp. **27**, 36990-37002 (2019).

70. Z. Liu, X. Lou, and J. Gao, “Deformation analysis of MEMS structures by modified digital moiré methods,” Opt. Lasers Eng. **48**, 1067-1075 (2010).

71. H. Xie, Z. Liu, D. Fang, F. Dai, H. Gao, and Y. Zhao, Y, “A study on the digital nano-moiré method and its phase shifting technique,” Meas. Sci. Technol. **15**, 1716 (2004).

72. Y. Xiao, Y. Cao, and Y. Wu, “Improved algorithm for phase-to-height mapping in phase measuring profilometry,” Appl. Opt. **51**, 1149-1155 (2012).

73. I. Yamaguchi and T. Zhang, “Phase-shifting digital holography,” Opt. Lett. **22**, 1268-1270 (1997).

74. J. M. Bioucas-Dias and G. Valadao, “Phase unwrapping via graph cuts,” IEEE Trans. Image Proc. **16**, 698-709 (2007).

75. H. Zhou, E. Stoykova, M. Hussain, and P. P. Banerjee, “Performance analysis of phase retrieval using transport of intensity with digital holography,” *invited paper*, Appl. Opt. **60**, A73-83 (2021).

76. L. Rao, F. Da, W. Kong, and H. Huang, “Flexible calibration method for telecentric fringe projection profilometry systems,” Opt. Exp. **24**, 1222-1237 (2016).

77. J. Villa, M. Araiza, D. Alaniz, R. Ivanov, and M. Ortiz, "Transformation of phase to (x, y, z)-coordinates for the calibration of a fringe projection profilometer," Opt. Lasers Eng. **50**, 256-261 (2012).

78. S. Zhang and P. S. Huang, "Novel method for structured light system calibration," Opt. Eng. **45**, 083601 (2006).

79. Z. Wang, M. Liu, S. Yang, S. Huang, X. Bai, X. Liu, J. Zhu, X. Liu, and Z. Zhang, "Precise full-field distortion rectification and evaluation method for a digital projector," Opt. Rev. **23**, 746-752 (2016).

80. I. Léandry, C. Brèque, and V. Valle, "Calibration of a structured-light projection system: development to large dimension objects," Opt. Lasers Eng. **50**, 373-379 (2012).

81. T. Borregaard, H. Nielsen, L. Nørgaard, and H. Have, "Crop-weed discrimination by line imaging spectroscopy," J. Agric. Eng. Res. **75**, 389-400 (2000).

82. B. Bordbar, H. Zhou, and P. P. Banerjee, "3D object recognition through processing of 2D holograms," Appl. Opt. **58**, G117-G186 (2019).

83. A. M. Wallace, P. Csákány, G. S. Buller, A. Walker, and S. Edinburgh, "3D imaging of transparent objects," Proc. British Machine Vision Conf. **8**, 46-77 (2000).

84. M. Locatelli, E. Pugliese, M. Paturzo, V. Bianco, A. Finizio, A. Pelagotti, P. Poggi, L. Miccio, R. Meucci, and P. Ferraro, "Imaging live humans through smoke and flames using far-infrared digital holography," Opt. Exp. **21**, 5379-5390 (2013).

85. N. J. Morris and K. N. Kutulakos, “Reconstructing the surface of inhomogeneous transparent scenes by scatter-trace photography,” Proc. Int. Conf. on Computer Vision 1-8 (2007).

86. M. Zhang, X. Lin, M. Gupta, J. Suo, and Q. Dai, “Recovering scene geometry under wavy fluid via distortion and defocus analysis,” Proc. Euro. Conf. on Computer Vision 234-250 (2014).

87. T. Kreis, *Handbook of Holographic Interferometry: Optical and Digital Methods*. John Wiley & Sons (2006).

88. A. M. Valm, S. Cohen, W. R. Legant, J. Melunis, U. Hershberg, E. Wait, A. R. Cohen, M. W. Davidson, E. Betzig, and J. Lippincott-Schwartz, “Applying systems-level spectral imaging and analysis to reveal the organelle interactome,” Nature **546**, 162-167 (2017).

89. T. Bonfort, P. Sturm, and P. Gargallo, “General specular surface triangulation,” Proc. Asia Conf. on Computer Vision 872-881 (2006)

90. L. Qieni, G. Baozhen, Y. Wenda, and Z. Yimo, “A method for measuring the thickness of transparent oil film on water surface using laser trigonometry,” Opt. Lasers Eng. **49**, 13-15 (2011).

91. K. N. Kutulakos, and E. A. Steger, “Theory of refractive and specular 3D shape by light-path triangulation,” Int’l. J. Computer Vision **76,** 13-24 (2008).

92. Z. Cui, J. Gu, B. Shi, P. Tan, and J. Kautz, “Polarimetric multi-view stereo,” Proc. IEEE Conf. on Computer Vision & Pattern Recognition 1558-1567 (2017).

93. D. Miyazaki, T. Shigetomi, M. Baba, R. Furukawa, S. Hiura, and N. Asada, “Surface normal estimation of black specular objects from multiview polarization images," Opt. Eng. **56**, 041303 (2016).

94. H. Murase, “Surface shape reconstruction of an undulating transparent object,” Proc. 3rd. Int’l. Conf. Computer Vision (1990).

95. N. J. Morris and K. N. Kutulakos, “Dynamic refraction stereo,” IEEE Trans. Pattern Anal. Machine Intelligence **33,** 1518-1531 (2011).

96. G. Eren, O. Aubreton, F. Meriaudeau, L. S. Secades, D. Fofi, A. T. Naskali, F. Truchetet, and A. Ercil, “Scanning from heating: 3D shape estimation of transparent objects from local surface heating,” Opt. Exp., **17**, 11457-11468 (2009).

97. W. Cai, X. Li, and L. Ma, “Practical aspects of implementing three-dimensional tomography inversion for volumetric flame imaging.,” Appl. Opt. **52**, 8106-8116 (2013).

98. M. B. Hullin, M. Fuchs, I. Ihrke, H. P. Seidel, and H. P. Lensch, “Fluorescent immersion range scanning,” ACM Trans. Graphics **27**, 87 (2008).

99. B. Atcheson, I. Ihrke, W. Heidrich, A. Tevs, D. Bradley, M. Magnor, and H. P. Seidel, “Time-resolved 3d capture of non-stationary gas flows,” ACM Trans. Graphics **27**, 1-9 (2008).

100. S. Osher, and R. Fedkiw, *Level Set Methods and Dynamic Implicit Surfaces*. Appl. Math. Sciences **153**. Springer (2006).

101. J. A. Sethian and P. Smereka, “Level set methods for fluid interfaces,” Annual Rev. Fluid Mech. **35**, 341-372 (2003).

102. B. Goldlucke, I. Ihrke, C. Linz, and M. Magnor, "Weighted minimal hypersurface reconstruction," IEEE Trans. Pattern Anal. Mach. Intell. **29,** 1194-1208 (2007).

103. K. Ikeuchi and D. Miyazaki, "Inverse polarization raytracing: Estimating surface shapes of transparent objects," IEEE Computer Soc. Conf. Computer Vision and Pattern Recognition (2005).

104. I. Ihrke, B. Goidluecke, and M. Magnor, "Reconstructing the geometry of flowing water," IEEE Int. Conf. Computer Vision **1**, 1055-1060 (2005).

105. A. Fitzgibbon, M. Pilu, and R. B. Fisher, "Direct least square fitting of ellipses," IEEE Trans. Pattern Anal. Machine Intelligence **21**, 476-480 (1999).

106. H. Guo, H. Zhou, and P. P. Banerjee, "Single-shot digital phase-shifting Moiré pattern for 3D metallic surface imaging," Digital Holography and Three-Dimensional Imaging Conf. HF3G-3 (2020).

107. H. Guo, H. Zhou, and P. P. Banerjee, "Single-shot digital phase-shifting Moiré patterns for 3D topography," Appl. Opt. **60**, A84-A92 (2021).

108. H. Guo, H. Zhou, and P. P. Banerjee, "Surface shape reconstruction of transparent objects using structured light," Digital Holography and Three-Dimensional Imaging Conf. (2021).

APPENDIX A

Matlab Code For Bi-Cylinder Simulation

```
%% Ray Propagation Model for Bi-cylinder Simulation Code
  % Written by Haiyun Guo
  %=================================================
  close all; clear all; clc;

%% Build Bi-cylinder Object
n = 1.5;                          % assumed refractive index
N = 4930; versize = 1256;         % horizontal & vertical axis lengths in pixels
R = N/2;
a = 0.000109301;                  % curvature parameter for paraboloids
h = 150;                          % distance between the edges of two paraboloids in pixels
c = 2*a*R^2+h;
Ref = zeros(versize,N);
Obj1 = zeros(versize,N);
Obj2 = zeros(versize,N);
for   j = 1:versize
   for   i = 1:N
         Ref(j,i) = 1+cos((i)/(226.8/2/pi));   % generate the reference patterns
         Obj1(j,i) = a*(i-R).^2;               % generate the bottom surface
         Obj2(j,i) = -a*(i-R).^2+c;            % generate the top surface
   end
end
figure; mesh(Obj1); hold on; mesh(Obj2); view(0,0);

%% Ray Propagation of the First Surface
figure; surfnorm(Obj1);           % draw normals of the bottom surface
[Nx,Ny,Nz] = surfnorm(Obj1);      % get the direction of the normal vector of each pixel
theta1 = atan(Nx./Nz);            % see in Figure 3-2
beta1 = asin(sin(theta1)/n);      % see in Figure 3-2
s1 = theta1-beta1;
s2 = 0.5*pi-s1;
k1 = tan(s2);
```

```
33
34  %% Ray Propagation of the Second surface
35  [Nx2,Ny2,Nz2] = surfnorm(Obj2);      % get the direction of the normal vectors
36  theta2 = atan(Nx2./Nz2);             % see in Figure 3-2
37  xx =    1:1:N;
38  y2= -a*(xx-R).^2+c;                  % cross-sectional curve of the top surface
39  H = (max(max(Obj2)))*ones(versize,N)-Obj2+5;    % distance from the incident plane to
40                                                   % the imaging plane, assuming d=5
41  delta = zeros(versize,N);            % define the translation array of rays in the
42                                       % imaging plane due to refraction in pixels
43  Rec = zeros(versize,N);              % define the record of final deformed image
44
45  %% Plot Ray Propagation Process of the Whole Object
46  figure;
47  for    j = 1:versize
48     for    i = 1:N
51          b = Obj1(j,i)-k1(j,i)*i;
52          y1 = k1(j,i)*xx+b;
53          [value,location] = min(abs(y2-y1));       % find intersections between refracted
54                                                    % rays and the top surface
55          plot(y2, 'linewidth',1); hold on; plot(y1,'linewidth',1); hold on;
56          plot( Obj1(1,:), 'linewidth',1); ylim([0 1500]); hold off;
57
58          alfa = theta2(j,location)-s1(j,i);
59          judge = n*sin(alfa);             % judge TIR or not
60          m = abs(judge);
61             if    m<1
62                beta = asin(judge);
63                ang = beta-alfa-s1(j,i);
64                delta(j,i) = H(j,location)*tan(ang);
65                x = round(location-delta(j,i));      % final imaging location of refracted rays
66                if (0<x)&&(x<=N)
67                      Rec(j,x) = Rec(j,x)+Ref(j,i);    % record the deformed intensity map
68                end
69             else
```

```
70                  zpoint = 1;
71              end
72              pause(0.001);               % for better view of plots
73              clf;
74      end
75  end
76
77  figure; imshow(Rec);
78  line = Rec(1,:);            % display the intensity distribution of one extracted deformed line
79  figure; plot(line);
```